



**CHALMERS**  
UNIVERSITY OF TECHNOLOGY

## The distribution of complex organic molecules in Barnard 5

Downloaded from: <https://research.chalmers.se>, 2026-07-10 12:41 UTC

Citation for the original published paper (version of record):

Carl, T., Wirström, E., Bergman, P. et al (2026). The distribution of complex organic molecules in Barnard 5. *Astronomy and Astrophysics*, 710. <http://dx.doi.org/10.1051/0004-6361/202558098>

N.B. When citing this work, cite the original published paper.

# The distribution of complex organic molecules in Barnard 5

T. Carl<sup>1</sup>\*, E. S. Wirström<sup>1</sup>, P. Bergman<sup>2</sup>, A. Punanova<sup>2</sup>, S. B. Charnley<sup>3</sup>, and A. O. H. Olofsson<sup>2</sup>

<sup>1</sup> Department of Physics and Astronomy, Chalmers University of Technology, 412 96 Gothenburg, Sweden

<sup>2</sup> Department of Physics and Astronomy, Chalmers University of Technology, Onsala Space Observatory, 439 92 Onsala, Sweden

<sup>3</sup> Astrochemistry Laboratory and the Goddard Center for Astrobiology, Mailstop 691, 8800 Greenbelt Road, Greenbelt, MD 20770, USA

Received 13 November 2025 / Accepted 13 April 2026

## ABSTRACT

Complex organic molecules (COMs) are prevalent in cold and dense molecular cloud environments and are formed by a combination of gas phase and grain surface chemical reactions. However, open questions remain about the exact formation pathways of many COMs and the desorption mechanisms of molecular ices at low temperatures. The aim of this study was to investigate the distribution of COMs in the area of the so-called methanol hotspot in the Barnard 5 dark cloud (B5-Hotspot) to better characterize the efficient desorption of COMs in that region, and to set observational constraints on the low-temperature formation of COMs. The IRAM 30 m and OSO 20 m telescopes were used to make pointed observations toward two positions close to B5-Hotspot, i.e., B5-Edge and B5-East 189, targeting transitions of CH<sub>3</sub>OH, CH<sub>3</sub>CHO, CH<sub>3</sub>OCHO, and CH<sub>3</sub>OCH<sub>3</sub>, as well as the five-atom COMs HCOOH and CH<sub>2</sub>CO. Emission from all the targeted COMs is detected toward both B5-Edge and B5-East 189. Non-LTE (local thermodynamic equilibrium) radiative transfer models for methanol do not suggest significant differences in the physical conditions of B5-Edge, B5-Hotspot, and B5-East 189, as probed by gas kinetic temperature  $T_k$  and H<sub>2</sub> volume density  $n(\text{H}_2)$ . However, the derived values of  $T_k$  and  $n(\text{H}_2)$  for B5-Hotspot using a new set of collisional rate coefficients differ significantly from previous estimates. Our results indicate that the efficient formation and desorption of COMs is not confined to B5-Hotspot, but is also active at the nearby positions B5-Edge and B5-East 189. When compared to COM data from the literature, our data supports a correlation between CH<sub>3</sub>OCHO and CH<sub>3</sub>OCH<sub>3</sub>, as well as the surface formation of CH<sub>3</sub>CHO by hydrogenation of CH<sub>2</sub>CO.

**Key words.** ISM: abundances – ISM: clouds – ISM: molecules

## 1. Introduction

Observations since the 1980s have shown that complex organic molecules (COMs), i.e., carbon-bearing molecules composed of at least six atoms, can reach significant gas phase abundances in cold ( $\sim 10$  K) and dense ( $> 10^5 \text{ cm}^{-3}$ ) molecular cloud environments. Early detections include acetaldehyde (CH<sub>3</sub>CHO; Matthews et al. 1985) and methanol (CH<sub>3</sub>OH; Friberg et al. 1988) toward TMC-1 and L134N. More recently, there have been additional detections of methyl formate (CH<sub>3</sub>OCHO) and dimethyl ether (CH<sub>3</sub>OCH<sub>3</sub>) in cold gas toward L1689B (Bacmann et al. 2012), L1544 (Vastel et al. 2014; Jiménez-Serra et al. 2016), and Barnard 5 (Taquet et al. 2017). In addition, survey studies of starless and prestellar cores in the Taurus and Perseus molecular clouds have shown that CH<sub>3</sub>CHO, CH<sub>3</sub>OCHO, and CH<sub>3</sub>OCH<sub>3</sub> can be found in many cold cores (Scibelli & Shirley 2020; Scibelli et al. 2024).

Experiments (e.g., Hiraoka et al. 1994; Bernstein et al. 2002; Fuchs et al. 2009; Nuevo et al. 2018; Ioppolo et al. 2021) and modeling efforts (e.g., Vasyunin et al. 2017; Jin & Garrod 2020; Garrod et al. 2022; Priestley et al. 2025; Borshcheva et al. 2025) strongly suggest that interstellar COMs are formed by interactions of gas phase atoms and molecules with microscopic dust grains, leading to the buildup of icy mantles around the refractory grains. Furthermore, the detection of gas phase COMs in cold and dense environments, not necessarily related to any ongoing or future star formation, indicates that (i) the process of COM formation starts before the onset of star formation,

and (ii) that ices are efficiently released into the gas phase by non-energetic desorption processes. In the current state-of-the-art astrochemical models, reactive desorption, i.e., the release of an ice species by its own energy of formation, is assumed to be the main driver of desorption in low-temperature environments.

In the case of CH<sub>3</sub>OH, i.e., the simplest and best studied COM, experiments, models, and observations indicate that its widespread distribution in the gas of molecular clouds down to visual extinctions of  $\sim 3$  mag can be well explained by the subsequent hydrogenation of CO at the surface of interstellar ices, followed by reactive desorption (e.g., Fuchs et al. 2009; Chuang et al. 2018; Scibelli & Shirley 2020; Punanova et al. 2022; Scibelli et al. 2024). However, the major formation routes of larger COMs, such as CH<sub>3</sub>OCHO and CH<sub>3</sub>OCH<sub>3</sub>, at low temperatures are generally not as well constrained as for CH<sub>3</sub>OH. In addition, and in contrast to CH<sub>3</sub>OH, there are potentially efficient gas phase reaction routes that can lead to the formation of larger COMs (Vasyunin & Herbst 2013; Balucani et al. 2015; Vasyunin et al. 2017; Skouteris et al. 2018).

The aim of this study is to investigate the distribution of COMs in the area around the methanol hotspot in the Barnard 5 (B5) dark cloud ( $d \approx 302$  pc; Zucker et al. 2018). This sets constraints on the desorption mechanism efficiently releasing COMs and water in that region, while setting additional constraints on low-temperature COM formation pathways. The B5 methanol hotspot (hereafter B5-Hotspot) is a cold and dense source ( $T_{\text{kin}} \approx 7.5$  K,  $n(\text{H}_2) \approx 2 \times 10^5 \text{ cm}^{-3}$ ; Taquet et al. 2017), located approximately 0.55 pc northwest of the prominent Class I protostar IRS-1, in a region that is not related to ongoing star

\* Corresponding author: tadeus.carl@chalmers.se

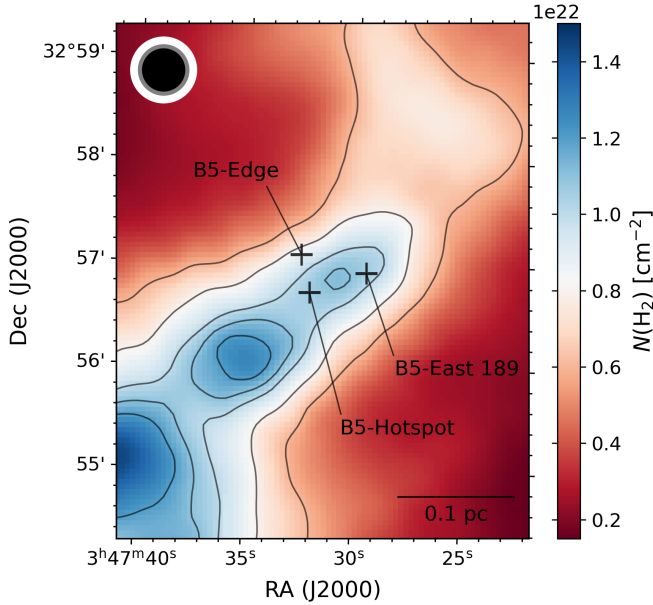


**Fig. 1.**  $\text{H}_2$  column density map created from HGBS (Herschel Gould Belt Survey; André et al. 2010; Roy et al. 2014) dust data for the region around the B5 methanol hotspot. The contours are  $N(\text{H}_2) = [0.6, 0.8, 1.0, 1.1, 1.2] \times 10^{22} \text{ cm}^{-2}$ . The targeted positions B5-Edge, B5-Hotspot, and B5-East 189 are marked with black crosses. The white, grey, and black circles in the top left show the approximate beam sizes of the OSO 20 m telescope at 96.7 GHz and the IRAM 30 m telescope at 85 GHz and 101 GHz, respectively.

formation (Wirström et al. 2014). It is located close to the center of an elongated ridge between two dense gravitationally unbound cores (Sadavoy 2013, Fig. 1). B5-Hotspot is the position of maximum gas phase methanol emission in the B5 dark cloud (see maps in Wirström et al. 2014; Taquet et al. 2017). Larger COMs, i.e.,  $\text{CH}_3\text{CHO}$ ,  $\text{CH}_3\text{OCHO}$ , and  $\text{CH}_3\text{OCH}_3$ , are identified at that position with gas phase abundances of  $\sim 10^{-10}$  (Taquet et al. 2017; Carl et al. 2023). Gas phase water is detected as well with a very high abundance of  $\sim 8 \times 10^{-9}$  (Wirström et al. 2014; Carl et al. 2023), which is about 50 times higher than the water abundance observed toward L1544 ( $\sim 1.4 \times 10^{-10}$ ; Caselli et al. 2012), the only other dark cloud source with a detection of cold gas phase water. Especially the high water abundance at B5-Hotspot indicates a very efficient release of ice species, as the gas phase water likely originates from deeper ice mantle layers, usually covered by CO- and  $\text{CH}_3\text{OH}$ -rich layers at the physical conditions established for the methanol hotspot (Tielens et al. 1991; Boogert et al. 2008, 2015). However, the nature of the efficient desorption remains elusive.

In general, thermal desorption, UV desorption, and cosmic ray desorption can be mostly ruled out as the main drivers, due to the low temperature and high density of the environment and to the localized peak emission of methanol at B5-Hotspot. Furthermore, explaining the efficient release of ice material via reactive desorption would require a process that is (locally) increasing surface reaction rates, and it is not clear what this process would be. One possible desorption mechanism might be collisional desorption driven by enhanced collisions between ice-covered grains, potentially due to a large-scale collision between cloud fragments or low-velocity shock waves propagating through the area. Kalvāns & Silsbee (2022) included collisional desorption in a simple astrochemical model and found that collisions are

potentially able to efficiently remove ice species from deeper mantle layers.

To better characterize the efficient desorption at B5-Hotspot, we made pointed observations with the IRAM 30 m and OSO 20 m telescopes toward two nearby positions, targeting the same set of gas phase COMs observed at B5-Hotspot, i.e.,  $\text{HCOOH}$ ,  $\text{CH}_2\text{CO}$ ,  $\text{CH}_3\text{CHO}$ ,  $\text{CH}_3\text{OCHO}$ , and  $\text{CH}_3\text{OCH}_3$ . Note that we loosely include the five-atom species formic acid ( $\text{HCOOH}$ ) and ketene ( $\text{CH}_2\text{CO}$ ) in the group of COMs. Studying the distribution of COMs in the area around B5-Hotspot, and whether or not the emission of other COMs peaks together with the methanol emission at that position, allows conclusions to be drawn about the spatial extent of the desorption. Furthermore, potential differences in gas phase COM abundances among the studied positions can reveal information about the molecular complexity of the releasing ices and the formation pathways of the COMs. To cover a range of physical conditions (as indicated by different  $N(\text{H}_2)$ ), we chose to study one position close to the edge of the B5 ridge, i.e., B5-Edge, while the other position is the dense core B5-East 189 (Fig. 1). The choice of the B5-East 189 position was based on the HGBS  $250 \mu\text{m}$  dust emission map ( $19''$  resolution) presented in Taquet et al. (2017), indicating an  $N(\text{H}_2)$  peak at our target position. However, as can be seen from Fig. 1, which is based on the HGBS  $N(\text{H}_2)$  map combining the dust emission maps at 160, 250, 350, and  $500 \mu\text{m}$  (Roy et al. 2014), the  $N(\text{H}_2)$  peak associated with the dense core B5-East 189 is slightly offset from our actually targeted position. However, considering the small differences in  $N(\text{H}_2)$  in this map as well as beam averaging effects and the high uncertainties related to the  $N(\text{H}_2)$  determination from dust emission, potential issues introduced by the offset of our B5-East 189 position relative to its  $N(\text{H}_2)$  peak are negligible.

The remaining paper is structured as follows. Sect. 2 covers the observational details of our study. Sect. 3 introduces the data analysis methods and presents the basic results. The results are then discussed in Sect. 4, and our main conclusions are drawn in Sect. 5.

## 2. Observations and data reduction

Using the IRAM 30 m telescope, we made pointed observations toward two positions, i.e., B5-Edge (03:47:32.5 RA, 32:57:05.0 Dec, J2000) and B5-East 189 (03:47:29.5 RA, 32:56:55.0 Dec, J2000), close to B5-Hotspot (03:47:32.1 RA, 32:56:43.0 Dec, J2000; Fig. 1). We targeted transitions of  $\text{HCO}^*$ ,  $\text{HCOOH}$ ,  $\text{CH}_2\text{CO}$ ,  $\text{CH}_3\text{CHO}$ ,  $\text{CH}_3\text{OCHO}$ , and  $\text{CH}_3\text{OCH}_3$  in the 3 mm band, including the  $\text{CH}_3\text{OH}(5_{-1}-4_0)$  transition at 84.521 GHz. Throughout this work, radicals such as  $\text{HCO}^*$  are marked with an asterisk. The  $\text{CH}_3\text{OH}(5_{-1}-4_0)$  transition turned out to be weakly masing at the physical conditions of B5-Edge and B5-East 189 (as also found for B5-Hotspot in Taquet et al. 2017). We therefore made additional pointed observations with the OSO 20 m telescope toward B5-Edge, B5-East 189, and B5-Hotspot, targeting further transitions of  $\text{CH}_3\text{OH}$  in the 3 mm band. In these observations we were furthermore covering the  $\text{C}^{18}\text{O}(1-0)$  transition at 109.782 GHz. A summary of all targeted transitions and their spectroscopic parameters can be found in Table D.1.

The target sources B5-Edge and B5-East 189 were observed with the IRAM 30 m telescope on 31 Dec 2022, 01 Jan 2023, and 02 Jan 2023 using the EMIR 090 heterodyne receiver in dual-polarization mode covering a total bandwidth of  $\sim 7.2$  GHz. The FTS50 backend was used with 50 kHz resolution and the four

sidebands covering frequency ranges of approx. 82.7–84.5 GHz, 86.3–88.1 GHz, 98.7–100.5 GHz, and 102.3–104.1 GHz. Pointing and focus was checked regularly on Mars or 0316+413. Position switching was used for the main observations with offset positions  $-10'$  RA from our target positions, splitting the observation time equally between on-source and off-source. Additional observations were made in frequency switching mode to confirm the offset positions are free of methanol emission. To increase the data sensitivity toward B5-Edge, additional observations were performed with the IRAM 30 m telescope on ten different occasions from October to December 2024 in the same setups as just described. In these observations, Uranus and 2251+158 were used as additional pointing and focus sources. In the 2022/2023 and 2024 observations, the system temperature ranged between  $\sim 70$  K and  $\sim 160$  K with an average of  $\sim 90$  K.

All three target positions B5-Edge, B5-Hotspot, and B5-East 189 were observed with the OSO 20 m telescope on 16, 17, and 18 May 2023 using a 4 mm dual-polarization sideband-separating SIS receiver covering a total bandwidth of  $\sim 4.8$  GHz (Walker et al. 2016). The backend was a FFT spectrometer with four sidebands and each sideband covering  $\sim 2.4$  GHz at  $\sim 95.8$ – $98.2$  GHz and  $\sim 107.8$ – $110.2$  GHz with a spectral resolution of 76.3 kHz. Pointing and focus was checked regularly on strong SiO masers. Position switching was used for the main observations with offset position at 03:47:50.00 RA, 32:58:00.0 Dec (J2000), splitting the observation time equally between on-source and off-source. Additional observations were made in frequency switching mode to confirm the offset position is free of methanol emission. The system temperature ranged between  $\sim 140$  K and  $\sim 780$  K with an average of  $\sim 285$  K.

The IRAM 30 m data was reduced with the CLASS/GILDAS<sup>1</sup> software and the OSO 20 m data was reduced with the 20 m data reduction software XS. We first removed spectra with artificial spikes (30 m data) and spectra with system temperature  $> 500$  K (20 m data), created average total spectra for the individual sidebands, corrected for frequency-dependent main beam efficiency<sup>2,3</sup> (30 m data: 0.79–0.81; 20 m data: 0.4–0.5), and subtracted suitable baseline fits. With the IRAM 30 m telescope, we reached an average on-source integration time of  $\sim 17$  h for B5-Edge and  $\sim 3.4$  h for B5-East 189. With the OSO 20 m telescope, we ended up with on source integration times of  $\sim 4.0$  h,  $\sim 3.6$  h, and  $\sim 3.8$  h for B5-Edge, B5-Hotspot, and B5-East 189, respectively. Using Python, and without smoothing the data, we then created  $12 \text{ km s}^{-1}$  wide spectral cutouts around the source LSR velocity ( $9.6 \text{ km s}^{-1}$ ) for each individual transition and calculated RMS noise levels over line-free channels. In our IRAM 30 m data, noise levels range between 1.4 mK and 2.5 mK for B5-Edge and 2.9 mK and 6.2 mK for B5-East 189, with mean values of 2.0 mK and 4.4 mK, respectively. In our OSO 20 m data, noise levels range between 12.1 mK and 26.0 mK with a mean of 17.8 mK.

### 3. Results and analysis

#### 3.1. Detected molecules and integrated intensities

Spectral lines are detected for all targeted molecules toward both B5-Edge and B5-East 189. Fig. D.1 shows a selection of

<sup>1</sup> <http://www.iram.fr/IRAMFR/GILDAS>

<sup>2</sup> <https://publicwiki.iram.es/Iram30-mEfficiencias>

<sup>3</sup> [https://www.chalmers.se/api/media/?url=https://cms.www.chalmers.se/Media/0agbppnl/oso\\_20-m\\_telescope\\_handbook\\_31aug2016.pdf](https://www.chalmers.se/api/media/?url=https://cms.www.chalmers.se/Media/0agbppnl/oso_20-m_telescope_handbook_31aug2016.pdf)

lines from our IRAM 30 m data for these two positions, and Fig. D.2 shows the detected lines of CH<sub>3</sub>OH and C<sup>18</sup>O from our OSO 20 m data for B5-Edge, B5-Hotspot, and B5-East 189. Table D.2 summarizes the measured line parameters, i.e., full width half maximum (FWHM), integrated intensity  $\int T_{\text{mb}} dv$ , and root mean square (RMS) noise level, for the three positions. Note that only transitions of CH<sub>3</sub>OH and C<sup>18</sup>O were targeted toward B5-Hotspot in this study. The FWHM are derived from Gaussian fits and RMS noise levels are calculated over line-free channels in  $12 \text{ km s}^{-1}$  wide spectral windows around the source LSR velocity. Integrated intensities are derived by summation over channels in  $2.0 \text{ km s}^{-1}$  wide windows around the LSR velocity for all COMs except CH<sub>3</sub>OH, for which we utilized  $2.6 \text{ km s}^{-1}$  windows. For HCO\* transitions, we use  $2.3 \text{ km s}^{-1}$  wide windows. For C<sup>18</sup>O(1–0), and because of the detected peak shoulders on the high-velocity side (see Fig. D.2), we calculate integrated intensities from the Gaussian fitting parameters rather than by summation over line channels. Upper limit integrated intensities are calculated for transitions without a securely detected spectral line, i.e., lines with  $T_{\text{mb}} < 3\sigma$ . The measured integrated intensities are used to calculate column densities  $N(X)$  for all detected molecules “X”, as described in Sects. 3.2 and 3.3.

#### 3.2. Non-LTE methanol analysis

Methanol population diagrams for the three target positions show significant divergence from a straight-line fit, indicating that the LTE (local thermal/thermodynamic equilibrium) approximation does not hold for this molecule. We therefore use the non-LTE, spherical radiative transfer code ALI (accelerated lambda iteration; Rybicki & Hummer 1991). The code was first used by Justanont et al. (2005) and later bench-marked by Maercker et al. (2008) and we use it to derive values for methanol column density (Eq. (A.1)), H<sub>2</sub> density,  $n(\text{H}_2)$ , and kinetic temperature,  $T_k$ . To account for the collisional excitation of methanol by *p*-H<sub>2</sub> we use the collisional rate coefficients calculated by Rabli & Flower (2010) (hereafter RF2010), and, for comparison, the rate coefficients recently published by Dagdigan (2024) (hereafter D2024). We present model results below for both these sets of collisional rate coefficients, since many rates differ substantially between the sets, especially for the E-type symmetry as can be seen in Fig. 4 of D2024. Our detected transitions are mainly of the E-type (see Table D.2).

##### 3.2.1. Models with RF2010 coefficients

For our models with the RF2010 rate coefficients, we mainly separate between two positions, i.e., B5-Hotspot and B5-East 189, while B5-Edge is considered as an off-center position toward the spherical B5-Hotspot model cloud. For both B5-Hotspot and B5-East 189, we assume a cloud radius of  $2 \times 10^{17}$  cm, corresponding to approximately half the width of the elongated ridge (i.e.,  $\sim 0.14$  pc; Fig. 1) in which both positions are located. We assume constant values of  $n(\text{H}_2)$ ,  $T_k$ , and methanol abundance  $X(\text{CH}_3\text{OH})$  inside the clouds and make model runs for  $T_k = [6.0, 10.0]$  K with a step size of 0.5 K, considering methanol energy levels up to 100 K. For each temperature, we sample  $\log[n(\text{H}_2)/\text{cm}^{-3}] = [4.9, 5.8]$  and  $\log[N(\text{E-CH}_3\text{OH})/\text{cm}^{-2}] = [13.3, 13.9]$ , using a step size of 0.02 for both parameters. We assume an A:E ratio of 1:1 and calculate  $N(\text{CH}_3\text{OH})$  as  $2 \times N(\text{E-CH}_3\text{OH})$ . We perform  $\chi^2$  analyses based on the integrated intensities of seven out of eight targeted methanol transitions, giving  $n = (7-2)$  degrees of freedom. In the RF2010 coefficient set, the rate coefficient for transitions between the E-levels 0<sub>0</sub> and

**Table 1.** Non-LTE methanol modeling results, CO depletion, and visual extinction.

Source	$\min(\chi_{\text{red}}^2)$	$T_{\text{ex}}$ (K)	$T_{\text{k}}$ (K)	$n(\text{H}_2)$ ( $\times 10^4 \text{ cm}^{-3}$ )	$N(\text{H}_2)^{\text{(a)}}$ ( $\times 10^{21} \text{ cm}^{-2}$ )	$X(\text{CH}_3\text{OH})$ ( $\times 10^{-8}$ )	$N(\text{CH}_3\text{OH})^{\text{(a)}}$ ( $\times 10^{13} \text{ cm}^{-2}$ )	$f_{\text{D}}^{\text{(b)}}$	$A_{\text{V}}^{\text{(c)}}$ (mag)
RF2010 collision coefficients, excluding the E-CH <sub>3</sub> OH(0 <sub>0</sub> -1 <sub>-1</sub> ) line at 108.894 GHz									
B5-Edge	2.5	2.8–7.9	8.0 <sup>+1.5</sup> <sub>-1.0</sub>	20.0 <sup>+13.2</sup> <sub>-8.7</sub>	43.7 <sup>+28.8</sup> <sub>-19.1</sub>	0.2 <sup>+0.1</sup> <sub>-0.1</sub>	7.5 <sup>+1.3</sup> <sub>-1.3</sub>	4.4	46
B5-Hotspot	0.7	2.8–7.9	8.0 <sup>+1.5</sup> <sub>-1.0</sub>	20.0 <sup>+13.2</sup> <sub>-8.7</sub>	67.0 <sup>+44.2</sup> <sub>-29.3</sub>	0.2 <sup>+0.1</sup> <sub>-0.1</sub>	11.5 <sup>+2.0</sup> <sub>-1.9</sub>	5.2	71
B5-East 189	1.0	2.9–7.4	7.5 <sup>+1.0</sup> <sub>-1.0</sub>	27.5 <sup>+13.2</sup> <sub>-11.7</sub>	92.2 <sup>+44.2</sup> <sub>-39.1</sub>	0.1 <sup>+0.1</sup> <sub>-0.0</sub>	10.2 <sup>+1.8</sup> <sub>-1.7</sub>	7.9	97
D2024 collision coefficients (reference models)									
B5-Edge	2.7	4.0–11.0	21 <sup>+19</sup> <sub>-7</sub>	1.6 <sup>+0.8</sup> <sub>-0.7</sub>	3.8 <sup>+1.8</sup> <sub>-1.6</sub>	1.6 <sup>+1.4</sup> <sub>-0.6</sub>	6.0 <sup>+1.4</sup> <sub>-1.0</sub>	0.5	4
B5-Hotspot	2.3	4.0–11.0	21 <sup>+19</sup> <sub>-7</sub>	1.6 <sup>+0.8</sup> <sub>-0.7</sub>	5.4 <sup>+2.6</sup> <sub>-2.3</sub>	1.6 <sup>+1.4</sup> <sub>-0.6</sub>	8.6 <sup>+2.0</sup> <sub>-1.4</sub>	0.6	6
B5-East 189	2.6	3.8–10.5	24 <sup>+19</sup> <sub>-7</sub>	1.3 <sup>+0.8</sup> <sub>-0.7</sub>	4.4 <sup>+2.3</sup> <sub>-2.0</sub>	1.7 <sup>+1.8</sup> <sub>-0.7</sub>	7.4 <sup>+1.3</sup> <sub>-1.5</sub>	0.6	5

**Notes.** <sup>(a)</sup> beam average column density, assuming a Gaussian 38'' beam (see Appendix B). <sup>(b)</sup> CO depletion factor, assuming  $^{16}\text{O}/^{18}\text{O} = 557$  (Wilson 1999) and  $X_{\text{ref}}(\text{C}^{16}\text{O}) = 2.7 \times 10^{-4}$  (Lacy et al. 1994). <sup>(c)</sup> Visual extinction, assuming all H is in H<sub>2</sub> and using  $A_{\text{V}} = N(\text{H}_2) [0.95 \times 10^{21}]^{-1} \text{ mag cm}^2$  (Whittet et al. 2007).

1<sub>-1</sub> (corresponding to the 108.894 GHz line) is zero and no collisional excitations or de-excitations occur between these levels. This is likely the cause why we had to exclude the 108.894 GHz line from the fitting. For the detected methanol lines, we assume calibration uncertainties of 10%, and for non-detected lines, we calculate  $1\sigma$  upper limit integrated intensities as input values for the integrated intensities and their uncertainties. For B5-Hotspot and B5-East 189, we find minimum  $\chi_{\text{red}}^2$  values of 0.7 and 1.0, respectively. In case of B5-Edge, we find a minimum of 2.5 for an offset of 0.65  $R$  from the center of the B5-Hotspot model cloud. The best-fit excitation temperatures of the modeled methanol transitions confirm the case of sub-thermal excitation for B5-Hotspot and B5-East 189, with the CH<sub>3</sub>OH(5<sub>-1</sub>-4<sub>0</sub>) line at 84.521 GHz having negative  $T_{\text{ex}}$  around  $-4.5$  K, which is in accordance with the results from Taquet et al. (2017) for B5-Hotspot and justifying the use of a non-LTE model.

### 3.2.2. Models with D2024 coefficients

For our models with the D2024 rate coefficients, we use the same modeling setup as with the RF2010 collision rates, only with adjusted ranges of  $\log[n(\text{H}_2)/\text{cm}^{-3}] = [3.4, 5.0]$ ,  $\log[N(\text{CH}_3\text{OH})/\text{cm}^{-2}] = [13.3, 13.8]$ , and  $T_{\text{k}} = [8, 85]$  K. We keep a step size of 0.02 for  $\log[n(\text{H}_2)]$  and  $\log[N(\text{E-CH}_3\text{OH})]$ , while for  $T_{\text{k}}$ , we use step sizes of 2–5 K with larger steps at higher temperatures. We consider methanol energy levels up to 100 K for  $T_{\text{k}} < 40$  K and all energy levels, i.e., up to 170 K, for  $T_{\text{k}} \geq 40$  K. The rate coefficient corresponding to the CH<sub>3</sub>OH(0<sub>0</sub>-1<sub>-1</sub>) line at 108.894 GHz is accounted for in the D2024 set, so we include it in the fitting, giving  $n = (8-2)$  degrees of freedom. For B5-Hotspot and B5-East 189, we find minimum  $\chi_{\text{red}}^2$  values of 2.3 and 2.6, respectively, while for B5-Edge, we find a minimum of 2.7 for an offset of 0.6  $R$  from the center of the B5-Hotspot model cloud. The modeled excitation temperatures of the considered methanol transitions are close to the ones obtained in the models using the RF2010 coefficient set, ranging between  $\sim 4$  K and  $\sim 11$  K, with the 84.521 GHz line having  $T_{\text{ex}}$  around  $-5$  K.

### 3.2.3. Model results and comparison

The results of our models are summarized in Table 1, and the uncertainty estimation is described in Appendix A. Beam average column densities for H<sub>2</sub> and CH<sub>3</sub>OH are derived from the best-fit values of  $n(\text{H}_2)$  and  $X(\text{CH}_3\text{OH})$  assuming a half power beam width of 38'', i.e., the approximate beam size of the OSO 20 m telescope at the strong  $\sim 96.7$  GHz CH<sub>3</sub>OH(2-1) lines. For B5-Edge, it is assumed that the telescope is pointed at an off-center position at 0.65  $R$  and 0.6  $R$  toward the B5-Hotspot model cloud for the models with the RF2010 and D2024 coefficient sets, respectively. See Appendix B for details on the used beam convolution method.

Using the RF2010 rate coefficients and within the uncertainties, our non-LTE modeling results for B5-Hotspot agree well with the results from the non-LTE analysis with RADEX reported in Taquet et al. (2017), i.e.,  $T_{\text{k}} = 7.5 \pm 1.5$  K,  $n(\text{H}_2) = (2.3 \pm 1.5) \times 10^5 \text{ cm}^{-3}$ , and  $N(\text{CH}_3\text{OH}) = (1.5 \pm 0.4) \times 10^{14} \text{ cm}^{-2}$ . Our derived methanol column density for B5-Hotspot also agrees with  $N(\text{CH}_3\text{OH})$  found in Wiström et al. (2014), i.e.,  $\sim 1.3 \times 10^{14} \text{ cm}^{-2}$ , using the ALI code. However, we find that utilizing the new set of collisional rate coefficients presented in D2024 significantly changes the derived best-fit values of  $n(\text{H}_2)$  and  $T_{\text{k}}$ . The D2024 rate coefficients tend to be larger than those calculated by RF2010, so it is expected to find a lower best-fit  $n(\text{H}_2)$ , which may also affect the best-fit  $T_{\text{k}}$ . Using the D2024 rate coefficients, we find 10–20 times lower  $n(\text{H}_2)$  and 2–3 times higher  $T_{\text{k}}$  compared to the case of using the RF2010 coefficients. A similar result regarding  $T_{\text{k}}$  is reported in Huang et al. (2025). Note that  $N(\text{CH}_3\text{OH})$  is rather insensitive to the choice of the rate coefficients as it is strongly constrained by the measured integrated intensities of the methanol lines. Therefore, within the uncertainties, the modeled  $N(\text{CH}_3\text{OH})$  for B5-Hotspot agrees with the modeled value from Taquet et al. (2017). We note that several of the downward collision rate coefficients involving the E-level 0<sub>0</sub> are not included in the set by RF2010 (see, e.g., the BASECOL<sup>4</sup> database; Dubernet et al. 2024), which strongly

<sup>4</sup> <https://basecol.vamdc.eu/>

affects the 108.894 GHz transition. Furthermore, the D2024 rate coefficients have been calculated (and tabulated) more densely at lower kinetic temperatures and are therefore more appropriate for the modeling of low-temperature environments. For these reasons, we adopt our models based on the newer set of rate coefficients as our reference models. The differing results of our non-LTE methanol models are further discussed in Section 4.2.

### 3.3. LTE column densities and abundances

Beam average column densities of  $C^{18}O$ ,  $HCO^*$ ,  $HCOOH$ ,  $CH_2CO$ ,  $CH_3CHO$ ,  $CH_3OCHO$ , and  $CH_3OCH_3$  are calculated assuming LTE conditions and optically thin emission (equations are given in Appendix C). It is further assumed that the emission fills the beam. The spectroscopic properties used for the LTE column density calculation are summarized in Table D.1 for all targeted molecular transitions. The spectroscopic data is mainly taken from the CDMS (Müller et al. 2005) and JPL (Pickett et al. 1998) catalogs. Derived molecular column densities are presented in Table D.3. Some specifications of the column density calculation are discussed in the following paragraphs.

In our reference non-LTE methanol models, the gas kinetic temperature is significantly higher than the excitation temperatures of the methanol lines, implying sub-thermal excitation. We therefore assume local thermal equilibrium conditions for all molecules listed above (excluding  $C^{18}O$ ) utilizing the average values of methanol  $T_{ex}$  for B5-Hotspot/B5-Edge and B5-East 189, i.e.,  $\sim 6.5$  K and  $\sim 7$  K, respectively (excluding the negative  $T_{ex}$  of the weakly masing 84.521 GHz line). For  $C^{18}O$ , we assume emission to be thermalized at the source kinetic temperatures, i.e.,  $T_{ex} = T_k$ , and therefore,  $T_{ex} = 21$  K for B5-Hotspot/B5-Edge and  $T_{ex} = 24$  K for B5-East 189. All utilized values of  $T_{ex}$  are summarized in Table D.3.

We create rotation diagrams for  $CH_3CHO$  for B5-Edge and B5-East 189 based on four detected transitions, and for  $CH_3OCHO$  for B5-East 189 based on six detected transitions (see Fig. D.3). The  $CH_3CHO$  rotation diagrams imply that LTE conditions are a good approximation for this molecule for both positions. The same was found for B5-Hotspot in Taquet et al. (2017) and Carl et al. (2023). Because of the goodness of the fits, we adopt the derived column densities for both positions. The narrow spread of  $E_u$  values for the considered transitions in the  $CH_3OCHO$  rotation diagram leads to a poor line fit, so for  $CH_3OCHO$ , we keep our assumption that  $T_{ex} = 7$  K for B5-East 189, and calculate its column density as described further below.

The rotational partition functions  $Q_{rot}(T_{ex})$  of the molecules are calculated as

$$Q_{rot}(T_{ex}) = Q_{rot}(9.375 \text{ K}) \left( \frac{T_{ex}}{9.375 \text{ K}} \right)^\alpha, \quad (1)$$

with  $\alpha = 1$  for linear rotors and  $\alpha = 3/2$  for asymmetric rotors. For  $CH_3CHO$ ,  $CH_3OCHO$ , and  $CH_3OCH_3$ , Einstein coefficients  $A_{ul}$  are calculated according to the JPL documentation<sup>5</sup>.

We assume the  $C^{18}O(1-0)$  line to be out of the optically thin limit, so we calculate its optical depth  $\tau_\nu$  iteratively for all three positions using

$$\tau_\nu = N(X) \left[ \frac{8\pi\nu^3}{c^3 A_{ul}} \frac{Q_{rot}}{g_u} \frac{E_u/T_{ex}}{e^{(h\nu/k_B T_{ex})} - 1} \Delta\nu \right]^{-1}, \quad (2)$$

<sup>5</sup> <https://spec.jpl.nasa.gov/ftp/pub/catalog/doc/catdoc.pdf>

where it is assumed that the optical depth does not vary significantly over the width  $\Delta\nu$  (FWHM) of the line. We calculate an initial estimate of  $\tau_\nu$  based on the column density derived from the optically thin approximation ( $N(X) = N_{thin}(X)$ ; Eq. (C.1)), as well as an initial estimate of the optical depth correction factor

$$f_{corr} = \frac{\tau_\nu}{1 - \exp(-\tau_\nu)}. \quad (3)$$

We then calculate the (corrected)  $C^{18}O$  column density as

$$N_{corr}(C^{18}O) = f_{corr} N_{thin}(C^{18}O). \quad (4)$$

The values of  $\tau_\nu$ ,  $f_{corr}$ , and  $N_{corr}(C^{18}O)$  are updated iteratively until the value of  $\tau_\nu$  converges (we use a tolerance of  $1 \times 10^{-6}$ ). The resulting (beam average) optical depth is  $\sim 0.4$  for all three target positions.

For the sake of comparison, we use ALI to calculate the peak optical depth of the  $C^{18}O(1-0)$  line through the center of the B5-Hotspot and B5-East 189 model clouds ( $R = 2 \times 10^{17}$  cm), using the best fit values of  $T_k$  and  $n(H_2)$  obtained from our reference non-LTE methanol models for both sources (see Sect. 3.2 and Table 1). Using this method, we find peak optical depths of  $\sim 0.3$  and  $\sim 0.2$  for B5-Hotspot and B5-East 189, respectively. Even though the effective (beam average) optical depth is approximately  $2/3$  the peak optical depth, the ALI-derived optical depths are generally in good agreement with the optical depths from the iterative method outlined above. In addition, the ALI models give best fit  $C^{18}O$  abundances of  $\sim 6 \times 10^{-7}$  and  $\sim 7 \times 10^{-7}$  for B5-Hotspot and B5-East 189, respectively, which agree reasonably well with the corrected  $C^{18}O$  abundances we obtain from the iterative method, i.e.,  $\sim 9 \times 10^{-7}$  and  $\sim 1 \times 10^{-6}$ , respectively. We therefore adopt the  $C^{18}O$  abundances derived from the iterative method for all three positions (see Table D.3). We also note that the ALI-derived excitation temperatures of the  $C^{18}O(1-0)$  line are  $\sim 24$  K and  $\sim 29$  K for B5-Hotspot and B5-East 189, respectively, supporting the assumption that  $C^{18}O$  emission is approximately thermalized at the gas kinetic temperature.

The column density of  $HCOOH$  is calculated as the sum of  $N(t-HCOOH)$  and  $N(c-HCOOH)$ . We find *cis/trans* (*c/t*) ratios of  $(7.2 \pm 0.8)\%$  and  $(3.2 \pm 1.8)\%$  for B5-Edge and B5-East 189, respectively.

$N(CH_2CO)$  is calculated from the detected *o*- $CH_2CO(5-4)$  line at 100.095 GHz assuming a statistical *ortho/para* (*o/p*) ratio of 3. Taquet et al. (2017) find an *o/p* ratio of  $3.3 \pm 1.2$  toward B5-Hotspot, while Bacmann et al. (2012) and Ohishi et al. (1991) report values of 3.3 and 3.5 for L1689B and TMC1, respectively.

For  $HCO^*$ ,  $CH_3OCHO$ , and  $CH_3OCH_3$ , we calculate total column densities by taking the average of the column densities determined for the individual detected lines. For the four  $HCO^*$  lines, the average differences from the column density means are 12% and 6% for B5-East 189 and B5-Edge, respectively. In case of  $CH_3OCHO$  for B5-East 189 (six lines), the average difference from the mean is 34%. Only two  $CH_3OCHO$  lines are detected for B5-Edge, and the corresponding column densities differ by 58%. In addition, only two  $CH_3OCH_3$  lines are detected for B5-East 189, with column densities differing by 78%. For B5-Edge, only one  $CH_3OCH_3$  line is detected and the total column density is calculated from that line. The spread in column densities calculated from the individual transitions could indicate non-LTE effects, adding to the uncertainties of the column density estimates.

For B5-Hotspot, we calculate the column density of  $HCO^*$  from unpublished data that was obtained with the OSO 20 m

telescope in May 2015. Without access to the raw data, we use tabulated Gaussian fitting parameters for the three strongest lines of HCO\* to calculate its average total column density.

We use  $N(\text{H}_2)$  and  $N(\text{CH}_3\text{OH})$  from our reference non-LTE methanol models to calculate molecular abundances relative to both  $\text{H}_2$  and  $\text{CH}_3\text{OH}$ . The abundances are summarized together with the column densities in Table D.3 and shown for all COMs and HCO\* in Fig. 2.

### 3.4. CO depletion factor

The CO depletion factor gives a quantitative estimate of the gas phase CO freeze-out onto interstellar dust grains. It compares a measured gas phase CO abundance  $X(\text{CO})$  toward a region of interest with a reference CO abundance  $X_{\text{ref}}(\text{CO})$ , supposed to be the gas phase abundance of interstellar CO in molecular cloud regions not characterized by CO freeze-out. The CO depletion factor  $f_{\text{D}}$  is generally calculated as

$$f_{\text{D}} = \frac{X_{\text{ref}}(\text{CO})}{X(\text{CO})}. \quad (5)$$

It follows that  $f_{\text{D}}$  will be always larger than one in regions that are characterized by CO freeze-out.

We calculate values of  $f_{\text{D}}$  from the abundances of C<sup>18</sup>O toward B5-Edge, B5-East 189, and B5-Hotspot. We assume an oxygen isotope ratio of  $^{16}\text{O}/^{18}\text{O} = 557$  (Wilson 1999) to calculate  $X(\text{C}^{16}\text{O})$ , and use the C<sup>16</sup>O reference abundance (with respect to  $\text{H}_2$ )  $X_{\text{ref}}(\text{C}^{16}\text{O}) = 2.7 \times 10^{-4}$  (Lacy et al. 1994; Punanova et al. 2022) to calculate the CO depletion factor via Eq. (5). We find  $f_{\text{D}} \approx 0.5$  for all three positions based on our reference non-LTE methanol models (see Table 1).

## 4. Discussion

### 4.1. Beam size effects

Because of the relatively small on-sky angular distances between the target positions ( $\sim 23''$  between B5-Hotspot and B5-Edge;  $\sim 35''$  between B5-Hotspot and B5-East 189), it is important to consider the effect of overlapping beams on the observed molecular emission. From the beam sizes listed in Table D.1, the largest effect is expected for  $\text{CH}_3\text{OH}$ , and the most intense  $\text{CH}_3\text{OH}$  lines are observed at  $\sim 96$  GHz, corresponding to a beam size of  $\sim 38''$ . The distribution of  $\text{CH}_3\text{OH}$  in the B5-Hotspot region is already known from gas phase maps presented in Wirström et al. (2014) and Taquet et al. (2017), and our non-LTE reference models for  $\text{CH}_3\text{OH}$  are in line with the overall results from these maps, indicating a decreasing  $N(\text{CH}_3\text{OH})$  from B5-Hotspot to B5-East 189 to B5-Edge.

In contrast to  $\text{CH}_3\text{OH}$ , there is no previous knowledge of the distribution of the other COMs targeted in this study, and it therefore becomes particularly important to consider the potential effect of overlapping beams when drawing conclusions about the overall distribution of those COMs in the B5-Hotspot region.  $\text{CH}_3\text{CHO}$  has the largest beam of all COMs other than  $\text{CH}_3\text{OH}$ , i.e.,  $\sim 27''$  on average, and therefore, the largest effect when discussing overlapping beams for the COMs. Assuming that the COM emission at B5-Hotspot is point-like and that a  $27''$  Gaussian beam is pointed toward B5-Edge, the picked up emission from B5-Hotspot would be  $\sim 13\%$ . Equivalently, for B5-East 189, the picked up emission from B5-Hotspot would be  $\sim 1\%$ . Those estimates can be considered as lower limits, as we do not expect COM emission to be point-like around B5-Hotspot. To obtain

upper limits for the overlapping beam effect, we assume a spherical model cloud of the same extent as for the non-LTE  $\text{CH}_3\text{OH}$  model ( $R = 44''$ ), centered at B5-Hotspot and with a constant  $\text{CH}_3\text{CHO}$  abundance of  $3.6 \times 10^{-10}$  (B5-Hotspot value; D.3). Using the same method as described in Appendix B, we then convolve this cloud with a  $27''$  Gaussian beam pointed at B5-Edge and B5-East 189 and calculate the column density  $N$  that would be measured at both positions. Comparing  $N$  to the maximum column density  $N_0$  when the beam is centered at B5-Hotspot gives  $N/N_0$  of  $\sim 0.8$  and  $\sim 0.5$  for B5-Edge and B5-East 189, respectively. Implications for the distribution of COMs in the B5-Hotspot area are discussed in Section 4.3.

### 4.2. Source physical conditions

Estimates of gas kinetic temperature  $T_{\text{k}}$  and  $\text{H}_2$  density  $n(\text{H}_2)$  for B5-Edge, B5-Hotspot, and B5-East 189 are derived from non-LTE radiative transfer models for  $\text{CH}_3\text{OH}$ . In our models, the B5-Edge position is considered as part of the B5-Hotspot model cloud, and since we assume a chemically and physically homogeneous medium, our estimates of  $T_{\text{k}}$  and  $n(\text{H}_2)$  are identical for B5-Hotspot and B5-Edge. When it comes to the B5-East 189 position, we find very similar values of  $T_{\text{k}}$  and  $n(\text{H}_2)$  (and also  $N(\text{CH}_3\text{OH})$ ) compared to B5-Hotspot. Minimizing the effect of overlapping beams (see previous section) by using higher resolution observations would result in more sensitive estimates of the source physical parameters. However, considering the large uncertainties related to both  $T_{\text{k}}$  and  $n(\text{H}_2)$ , it is unlikely that higher resolution observations would result in significant differences in  $T_{\text{k}}$  and  $n(\text{H}_2)$  between B5-Hotspot and B5-East 189.

We obtain significantly different results for  $T_{\text{k}}$  and  $n(\text{H}_2)$  depending on the used collisional rate coefficients. Using the new set of rate coefficients recently reported in D2024 gives 2–3 times higher  $T_{\text{k}}$  and 10–20 times lower  $n(\text{H}_2)$  compared to the case of using the rate coefficients from RF2010. Our model results indicate that kinetic temperature estimates for sources in the literature, which are based on non-LTE methanol models utilizing the RF2010 rate coefficients, might be underestimated. To make a more direct comparison to the models with the D2024 coefficients, we created another set of models using the D2024 coefficients and excluded the E- $\text{CH}_3\text{OH}(0_0-1_{-1})$  line at 108.894 GHz from the fitting. For B5-Hotspot, we find best-fit values of  $T_{\text{k}} = 19(+66, -11)$  K and  $n(\text{H}_2) = 1.8(+2.9, -1.4) \times 10^4 \text{ cm}^{-3}$ . At a comparable  $\chi_{\text{red}}^2$  minimum of 2.8, those values are very close to the best fit values obtained when the 108.894 GHz line is included (Table 1), but the uncertainties increase significantly. The same is observed for the B5-East 189 models. We checked molecular line data bases for lines that would potentially overlap with the 108.894 GHz methanol line, but were not able to identify any candidates that might affect our measured integrated intensity in this source region. Further investigations into the details of methanol excitation are beyond the scope of this paper, but it would be worthwhile to conduct in-depth observational studies on this subject utilizing more  $\text{CH}_3\text{OH}$  lines from a wider range of upper state energies.

The HGBS  $N(\text{H}_2)$  map presented in Fig. 1 suggests a beam average  $N(\text{H}_2)$  between  $\sim 0.8 \times 10^{22} \text{ cm}^{-2}$  for B5-Edge and  $\sim 1 \times 10^{22} \text{ cm}^{-2}$  for B5-Hotspot and B5-East 189. Our derived values of  $N(\text{H}_2)$  are in much better agreement with those estimates when using the D2024 rate coefficients. Based on the modeled  $N(\text{H}_2)$  values and assuming that all gas phase hydrogen is bound in  $\text{H}_2$ , we calculate the corresponding visual extinction as

$$A_{\text{V}} = N(\text{H}_2) \left[ 0.95 \times 10^{21} \right]^{-1} \text{ mag cm}^2 \quad (6)$$

(Whittet et al. 2007). In general, values of  $A_V \sim 5$  resulting from our models with the D2024 rate coefficients appear more reasonable for this source region than  $A_V \sim 50-100$  (see Table 1).

Taquet et al. (2017) discussed that the efficient release of ice material at the position of B5-Hotspot might be induced by enhanced grain-grain collisions, potentially caused by a cloud-cloud collision or low-velocity shock waves. The HGBS dust temperature map for the B5-Hotspot region implies  $T_{\text{dust}} \approx 13$  K. Our modeled values of  $T_k \approx 20$  K might be a relic of such a large scale collision event or a shock wave propagating through the area as the dust is expected to cool more efficiently than the gas by means of evaporative cooling due to the release of ice material. However, the lower bounds of our modeled  $T_k$  uncertainty are close to 15 K, which would imply an approximate temperature equilibrium between gas and dust. To better assess our modeled  $T_k$ , we took a CO(1–0) spectrum toward B5-Hotspot with the OSO 20 m telescope in October 2025 (see Fig. D.3). The peak  $T_{\text{mb}}$  of this optically thick emission line gives a lower bound to the source  $T_k$  and is measured as  $22 \pm 2$  K, which is similar to the modeled  $T_k$  when utilizing the D2024 rate coefficients, and indicates that the gas kinetic temperature is indeed higher than the dust temperature.

The CO depletion toward our target positions is  $<1$ , which is considered as a non-physical result in regions where we expect CO to be (at least partly) frozen out onto dust grains. Even though we do expect that, for example, a past grain heating event has released a large amount of ice species into the gas phase in the B5-Hotspot area, we also expect a significant amount of freeze-out back onto grains. Evidence for this comes from the measured gas phase  $\text{CH}_3\text{OH}/\text{H}_2\text{O}$  ratio for B5-Hotspot of  $\sim 1.3$  (assuming  $N(\text{H}_2\text{O}) \approx 6.6 \times 10^{13} \text{ cm}^{-2}$ ; Taquet et al. 2017), which is much higher than what can be expected for the ice  $\text{CH}_3\text{OH}/\text{H}_2\text{O}$  ratio, usually measured to be around 0.01–0.14 in cold and dense molecular cloud sources (Boogert et al. 2011; Chiar et al. 2011; Chu et al. 2020; Goto et al. 2021; McClure et al. 2023). It should be noted, however, that the uncertainty related to the utilized CO reference abundance is high (Lacy et al. 1994; Puananova et al. 2022), and considering a higher  $X_{\text{ref}}(\text{CO})$  close to its upper bound of  $9.1 \times 10^{-4}$  yields  $f_D > 1$  for all three considered positions. In general, the very similar values of  $f_D$  ( $\sim 0.5$  for all three sources) are likely effected by overlapping beams (see Sect. 4.1), especially considering the relatively large  $\text{C}^{18}\text{O}$  beam of  $\sim 34''$ .

An interesting consequence of a potential past heating event is the creation of an unusual ice mantle structure in the B5-Hotspot area due to the subsequent freeze-out of gas phase species. It is often assumed that ice mantles in dense molecular clouds show at least a two-phase layering with a bottom layer dominated by  $\text{H}_2\text{O}$  and a top layer dominated by CO and  $\text{CH}_3\text{OH}$  (Cuppen et al. 2011; Boogert et al. 2015; Penteadó et al. 2015; Müller et al. 2021). If these layers are (partly) removed during a heating event, freeze-out during cooling would create a top ice layer in which  $\text{CH}_3\text{OH}$ ,  $\text{H}_2\text{O}$ , and CO, for example, are well mixed. This could have important consequences for the efficiency of certain grain-surface reactions as we discuss in the next section. The assumption of layered ices was also recently challenged by dark cloud observations toward background stars with the JWST by McClure et al. (2023), indicating that the upper ice layers in their target sources contain both  $\text{H}_2\text{O}$  and  $\text{CH}_3\text{OH}$ .

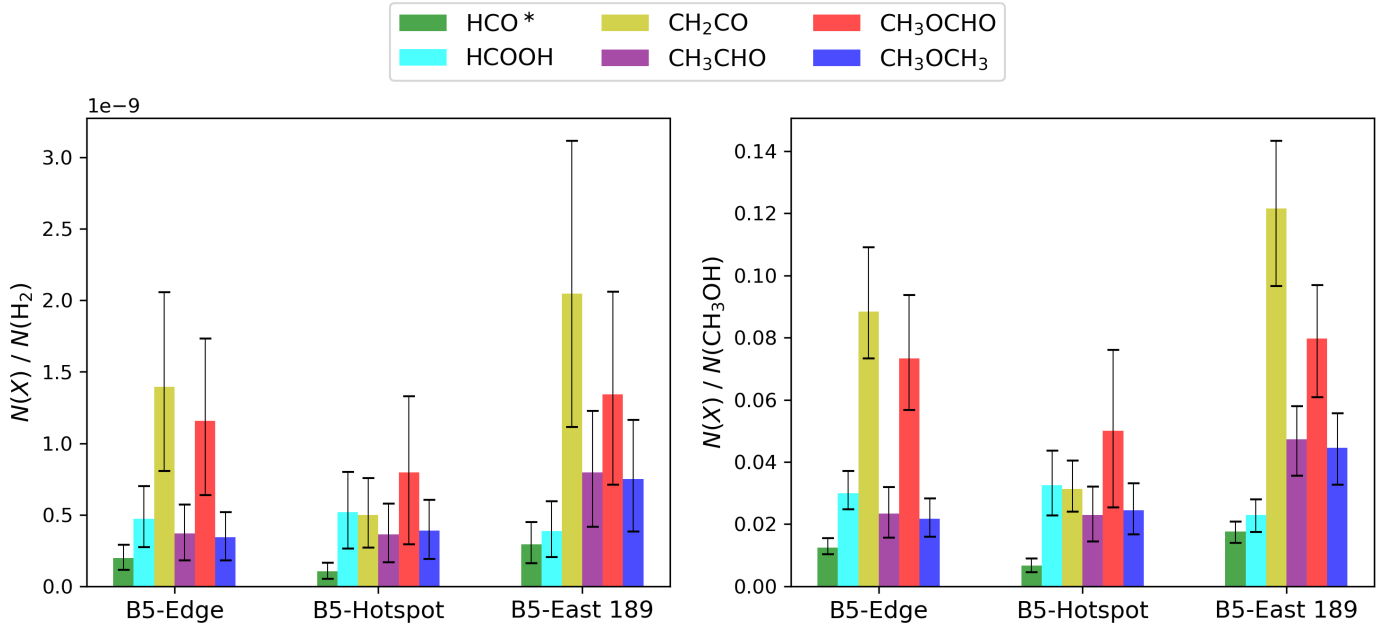
#### 4.3. COM distribution

Considering the effects from overlapping beams, our three target positions are not fully independent, but the measured emission

is shared to some degree between B5-Edge and B5-Hotspot as well as between B5-East 189 and B5-Hotspot. In Section 4.1, we estimated that the measured COM column densities at B5-Edge would be  $\sim 0.8$  of the respective peak column densities at B5-Hotspot, if the COMs were homogeneously distributed in a spherical model cloud centered at B5-Hotspot and extending over the width of the B5 ridge (0.14 pc). At B5-East 189, they would be up to  $\sim 0.5$  of the peak column densities at B5-Hotspot. Ratios of measured column densities at B5-Edge and B5-Hotspot are all close to, or considerably higher than, 0.8, which would be expected from our ridge-wide model cloud (see Table D.3). This confirms that the emission of COMs is extended toward the B5-Edge position. For  $\text{CH}_2\text{CO}$ ,  $N(X)/N(X)_{\text{hotspot}} = 2.0 \pm 0.3$ , clearly indicating that most  $\text{CH}_2\text{CO}$  emission must originate closer to the B5-Edge position rather than from B5-Hotspot. Making the same direct comparison of measured column densities for B5-East 189 (see Table D.3), ratios are significantly larger than 0.5 for all COMs except  $\text{HCOOH}$ , showing that the COM emission in the B5-Hotspot region is indeed higher toward the B5-East 189 position than toward B5-Hotspot itself. Here  $\text{CH}_2\text{CO}$  also has an exceptionally high  $N(X)/N(X)_{\text{hotspot}}$  of  $3.3 \pm 0.6$ . The high ratios for  $\text{CH}_2\text{CO}$  indicate that most  $\text{CH}_2\text{CO}$  emission measured at B5-Hotspot could be picked up from B5-Edge and B5-East 189.

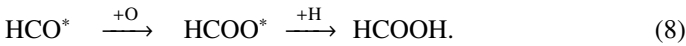
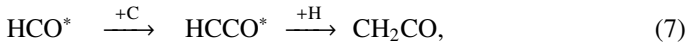
Overall, our observations toward B5-Edge and B5-East 189 demonstrate that gas phase COMs ( $\text{HCOOH}$ ,  $\text{CH}_2\text{CO}$ ,  $\text{CH}_3\text{CHO}$ ,  $\text{CH}_3\text{OCHO}$ ,  $\text{CH}_3\text{OCH}_3$ ) are extended in the region around B5-Hotspot, and especially toward B5-East 189 in the northeast, where we observe the highest COM column densities and abundances. This justifies our assumption that the observed molecular emission is filling the beam. Furthermore, our data shows that COM emission does not follow the emission distribution of  $\text{CH}_3\text{OH}$ , which peaks at B5-Hotspot. This indicates that the efficient desorption of ices at B5-Hotspot is (or was) also active at B5-Edge and B5-East 189. The offset between the  $\text{CH}_3\text{OH}$  peak at B5-Hotspot and the COM peak at B5-East 189 could be explained by a more complex ice composition at B5-East 189 compared to B5-Hotspot, with higher abundances of COMs relative to  $\text{CH}_3\text{OH}$ . That is, if it is assumed that  $\text{CH}_3\text{OH}$  is partly consumed in the formation of larger COMs at the surface of ice-covered grains. Alternatively, one could assume a similar ice composition at B5-Hotspot and B5-East 189, and then partial consumption of  $\text{CH}_3\text{OH}$  to form larger COMs in the gas phase with higher efficiencies at B5-East 189. However, it is not possible to distinguish between these two scenarios based on the limited physical data for B5-Hotspot and B5-East 189. Ice observations toward the region around B5-Hotspot would be highly valuable to better characterize the desorption and chemical evolution of this interesting source.

Fig. 2 shows the molecular abundances of  $\text{HCO}^*$  and COMs with respect to  $\text{H}_2$  (left) and with respect to  $\text{CH}_3\text{OH}$  (right). The measured abundances show barely significant differences between the three considered positions, especially in the case of the abundances with respect to  $\text{H}_2$  and likely affected by overlapping beams. More significant differences can be noted for the abundances with respect to  $\text{CH}_3\text{OH}$  due to the smaller uncertainty related to  $N(\text{CH}_3\text{OH})$ . The relative abundances of the larger COMs  $\text{CH}_3\text{CHO}$ ,  $\text{CH}_3\text{OCHO}$ , and  $\text{CH}_3\text{OCH}_3$  are very similar among the three positions, which might be indicative of a shared physical and chemical evolution. Contrary to that, we observe clear differences in the relative abundances of the five-atom COMs  $\text{HCOOH}$  and  $\text{CH}_2\text{CO}$ , with  $\text{CH}_2\text{CO}$  being 3–4 times more abundant than  $\text{HCOOH}$  at B5-Edge and B5-East 189, while both molecules are similarly abundant at B5-Hotspot. Such differences could in principle be due to a higher atomic C/O ratio at



**Fig. 2.** Abundances of COMs formic acid (HCOOH), ketene (CH<sub>2</sub>CO), acetaldehyde (CH<sub>3</sub>CHO), methyl formate (CH<sub>3</sub>OCHO), and dimethyl ether (CH<sub>3</sub>OCH<sub>3</sub>) with respect to H<sub>2</sub> (left panel) and CH<sub>3</sub>OH (right panel) for B5-Edge, B5-Hotspot, and B5-East 189. Abundances of the important COM precursor radical HCO\* are also shown. For B5-Hotspot, column densities of HCOOH, CH<sub>2</sub>CO, CH<sub>3</sub>OCHO, and CH<sub>3</sub>OCH<sub>3</sub> are from Taquet et al. (2017), and the column density of CH<sub>3</sub>CHO is from Carl et al. (2023). The column density of HCO\* for B5-Hotspot was calculated from unpublished data obtained with the OSO 20 m telescope (see Section 3.3).

B5-Edge and B5-East 189 compared to B5-Hotspot, considering that CH<sub>2</sub>CO and HCOOH have efficient surface formation routes via reactions of HCO\* with C and O, respectively, followed by hydrogenation, i.e.,



An alternative explanation might be that, relative to B5-Edge and B5-East 189, CH<sub>2</sub>CO is more efficiently hydrogenated to CH<sub>3</sub>CHO at B5-Hotspot. However, we do not observe an elevated abundance of CH<sub>3</sub>CHO at B5-Hotspot relative to B5-Edge and B5-East 189, as would be expected in such a scenario. A possible source of error could arise from using the statistical *o/p* ratio of 3 in the calculation of  $N(\text{CH}_2\text{CO})$  for B5-Edge and B5-East 189. The *o/p*-CH<sub>2</sub>CO ratio is not constrained at these positions because we only have one *o*-CH<sub>2</sub>CO line detected. However, Taquet et al. (2017) report a measured *o/p* ratio of  $3.3 \pm 1.2$  for B5-Hotspot.

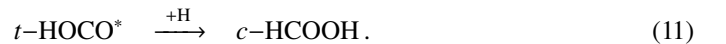
We observe systematically higher CH<sub>3</sub>OCHO abundances than CH<sub>3</sub>OCH<sub>3</sub> abundances. This might support the formation pathway suggested in Balucani et al. (2015) in which CH<sub>3</sub>OCHO is indirectly formed from CH<sub>3</sub>OCH<sub>3</sub> via the gas phase reactions



In general, a more complex gas phase chemistry could be expected for the B5-Hotspot region, comparing to cold sources with less efficient desorption (see also Sect. 4.4).

Taquet et al. (2017) report a highly non-equilibrium *c/t*-HCOOH ratio of ~6% toward B5-Hotspot. We also observe

elevated *c/t* ratios of ~7% and ~3% toward B5-Edge and B5-East 189, respectively. Quantum chemical calculations conducted by García de la Concepción et al. (2022) demonstrate that, at ISM conditions, almost all HCOOH should be in its lower energy *trans*-configuration. This study also presents measured non-equilibrium *c/t* ratios for several ISM sources and predicts a *c/t* ratio of  $< 10^{-50}$  for B5-Hotspot (!). Taquet et al. (2017) suggest that the elevated *c/t* ratio in the B5-Hotspot area and other ISM sources might be due to the formation of significant amounts of *c*-HCOOH from the low-energy *trans*-isomer of the HOCO\* radical via surface reaction



The formyl radical (HCO\*) is observed in the gas phase toward all three positions. While HCO\* can be formed in the gas through electron dissociative recombination of protonated formaldehyde (Hamberg et al. 2007), it can also be produced on grain surfaces (from CO) where it is an important COM precursor. Here we assume the latter formation scenario and hence that HCO\* is involved to some degree in the formation of all the COMs considered in this study. HCO\* has been detected toward several cold molecular cloud sources such as TMC-1, TMC-2, and B1-b (Cernicharo et al. 2012; Agúndez et al. 2015; Bacmann & Faure 2016). Column densities of HCO\* in these sources are on the order of  $10^{11} - 10^{13} \text{ cm}^{-2}$ , and the column densities toward our target sources fall in this range. Bacmann & Faure (2016) studied typical ratios of HCO\*:H<sub>2</sub>CO:CH<sub>3</sub>O\*:CH<sub>3</sub>OH for a set of eight prestellar cores in Taurus (5), Ophiuchus (2), and Aquila (1) and find values of CH<sub>3</sub>OH:HCO\* of ~9–26 with a mean of ~15. The ratios of CH<sub>3</sub>OH:HCO\* for B5-Edge, B5-Hotspot, and B5-East 189 are approximately 80, 150, and 60, respectively. These high values are largely due to a systematically

higher  $N(\text{CH}_3\text{OH})$  as compared to the prestellar cores studied in [Bacmann & Faure \(2016\)](#). The higher  $N(\text{CH}_3\text{OH})$  might be due to differences in source structure and age, comparing our sources with prestellar cores, as well as due to the very efficient release of methanol at B5-Hotspot, most likely also affecting B5-Edge and B5-East 189. However, comparing  $\text{CH}_3\text{OH}$  column densities for a collection of starless and prestellar cores in Taurus (31 cores; [Scibelli & Shirley 2020](#)) and to a similar dataset in Perseus (35 cores; [Scibelli et al. 2024](#)), it appears there are significant differences between the two clouds with an average  $\text{CH}_3\text{OH}$  column density about five times higher in Perseus. In addition, as we discuss below, our  $\text{CH}_3\text{OH}$  column densities are on a similar level for the sampled cores in Perseus, so the high  $\text{CH}_3\text{OH}:\text{HCO}^*$  ratios when compared to the [Bacmann & Faure \(2016\)](#) set might rather be due to chemical differences between the host molecular clouds than due to differences in source structure and age. However, at least the very high  $\text{CH}_3\text{OH}:\text{HCO}^*$  ratio of  $\sim 150$  at B5-Hotspot might indeed be interpreted as an expression of the very efficient desorption, clearly constrained at that position by the high gas phase  $\text{H}_2\text{O}$  abundance.

Experiments by [Pirim & Krim \(2011\)](#) showed that the presence of  $\text{H}_2\text{O}$  has a catalytic effect on the surface formation of  $\text{H}_2\text{CO}$  and  $\text{CH}_3\text{OH}$  from CO. As mentioned above, the efficient release of ice species from the dust grains in the B5-Hotspot region followed by a partial freeze-out back onto grains would lead to an untypical ice composition in the top mantle layers, where  $\text{CH}_3\text{OH}$  would be mixed with both  $\text{H}_2\text{O}$  and CO. Therefore, according to the findings of [Pirim & Krim \(2011\)](#), the surface formation of both  $\text{H}_2\text{CO}$  and  $\text{CH}_3\text{OH}$  might be enhanced in the area around B5-Hotspot.

#### 4.4. Comparison to other sources

[Fig. 3](#) shows a comparison between our measured  $\text{CH}_3\text{OH}$  column densities and abundances and the  $\text{CH}_3\text{OH}$  data from a survey by [Scibelli et al. \(2024\)](#), covering a sample of 35 starless and prestellar cores in Perseus. Green bars are marking sources where only  $\text{CH}_3\text{OH}$  is detected and blue bars are marking sources where at least  $\text{CH}_3\text{CHO}$  is detected as well. The dashed green and blue lines mark the mean of the two sample sets, while the dashed black line marks the mean of the whole Perseus sample (excluding our measured values in all cases). Note that two cores in this sample, i.e., cores 799 and 800, are located in the southern part of the B5 dark cloud. Note also that [Scibelli et al. \(2024\)](#) use the HGBS  $N(\text{H}_2)$  data to calculate abundances. As mentioned before, our modeled  $N(\text{H}_2)$  values are in reasonable agreement with the HGBS data, especially considering the high uncertainties related to the determination of  $N(\text{H}_2)$ , so our abundances with respect to  $\text{H}_2$  are generally comparable to those in the Perseus sample. As already pointed out in [Scibelli et al. \(2024\)](#), higher  $\text{CH}_3\text{OH}$  column densities and abundances seem to correlate with a higher chemical complexity of the cores, as traced here by the additional detection of  $\text{CH}_3\text{CHO}$  in 15/35 cores of the Perseus sample. We measure  $\text{CH}_3\text{OH}$  abundances that are significantly above the total average of the Perseus sample, and even above the average of the COM-rich cores. However, our measured column densities are close to the total average, but significantly below the average of the COM-rich cores. This might be evidence for the very efficient release of  $\text{CH}_3\text{OH}$  and other ice species in the B5-Hotspot area.

In [Fig. 4](#), we compare our measured column densities and abundances of the larger COMs  $\text{CH}_3\text{CHO}$ ,  $\text{CH}_3\text{OCHO}$ , and

$\text{CH}_3\text{OCH}_3$  to the data of those 15/35 cores in the [Scibelli et al. \(2024\)](#) survey in which at least  $\text{CH}_3\text{CHO}$  is detected alongside  $\text{CH}_3\text{OH}$ . Upper limits are indicated by transparent bars and the dashed purple, red, and blue lines mark the average values obtained for the Perseus sample. Considering that only 3/35 cores in the sample show emission from all three large COMs, it is remarkable that we observe emission from all of them across the whole northern B5 ridge around B5-Hotspot, especially since only  $\text{CH}_3\text{CHO}$  is detected toward cores 799 and 800 in the southern part. These observations support the model predictions of [Priestley et al. \(2025\)](#) that COMs can be actively formed in molecular clouds starting from densities of a few  $10^3 \text{ cm}^{-3}$ , prior to any core formation. Abundances of  $\text{CH}_3\text{OCHO}$  with respect to  $\text{H}_2$  toward the B5 ridge are significantly above the Perseus average, while abundances of  $\text{CH}_3\text{CHO}$  are close to average, or, in case of B5-East 189, slightly above average. The very high  $\text{CH}_3\text{OCH}_3$  abundance of core 627 drastically elevates the mean of the sample set, while the abundances of cores 264, 321, and 326 are more comparable to our measured abundances. The fact that we do observe  $\text{CH}_3\text{OCHO}$  abundances that are systematically higher than the Perseus average, as well as higher than  $\text{CH}_3\text{OCH}_3$  abundances, might indicate efficient gas phase conversion of  $\text{CH}_3\text{OCH}_3$  to  $\text{CH}_3\text{OCHO}$  in the B5-Hotspot region, according to reactions (9) and (10).

Assuming that COMs are mostly formed by surface reactions and released with comparable efficiencies, gas phase COM abundances with respect to  $\text{CH}_3\text{OH}$  should give an idea of the complexity of releasing ices. Measured abundances of larger COMs with respect to  $\text{CH}_3\text{OH}$  toward the B5 ridge are significantly below or, in case of  $\text{CH}_3\text{OCHO}$ , comparable to the mean of the Perseus sample, which might be an indication for a lower ice chemical complexity in the B5-Hotspot region. This might be explained by a physically and chemically less evolved stage of the B5-Hotspot region relative to the more evolved starless and prestellar cores of the Perseus sample. A lower ice chemical complexity in the B5-Hotspot region might be further supported by the significantly lower column densities of  $\text{CH}_3\text{OH}$  and larger COMs compared to the Perseus cores. The high abundances of COMs with respect to  $\text{H}_2$  toward the B5 ridge might then be interpreted as an indication of the overly efficient release of generally less complex ices in the B5-Hotspot area.

[Scibelli et al. \(2024\)](#) note that the three cores that are showing emission from all three large COMs, i.e., cores 264, 321, and 326, are located in the active and shocked region NGC1333, so desorption might be partly caused by thermal processes induced by shocks or outflow interactions, for example. They further note that non-LTE RADEX models for  $\text{CH}_3\text{OCHO}$  indicate that  $T_k \approx 20 \text{ K}$  for cores 264 and 326, while their RADEX  $\text{CH}_3\text{OH}$  models indicate  $T_k \approx 5\text{--}10 \text{ K}$ . Based on the discussion of our non-LTE  $\text{CH}_3\text{OH}$  models utilizing the rate coefficients of both [RF2010](#) and [D2024](#), it is feasible that  $T_k$  of cores 264 and 326 is actually closer to 20 K than to 5–10 K, making it more comparable to the  $T_k$  that we derive for our target positions.

#### 4.5. COM relations

Several observational studies of low-mass and high-mass protostellar objects demonstrated that the abundances of  $\text{CH}_3\text{OCHO}$  and  $\text{CH}_3\text{OCH}_3$  are highly correlated over an abundance range that spans  $\sim 6$  orders of magnitude (e.g., [Bisschop et al. 2007](#); [Jaber et al. 2014](#); [Rivilla et al. 2017](#); [Coletta et al. 2020](#); [Yang et al. 2021](#)). This is often interpreted as an indication that either the two molecules share a common precursor or that one

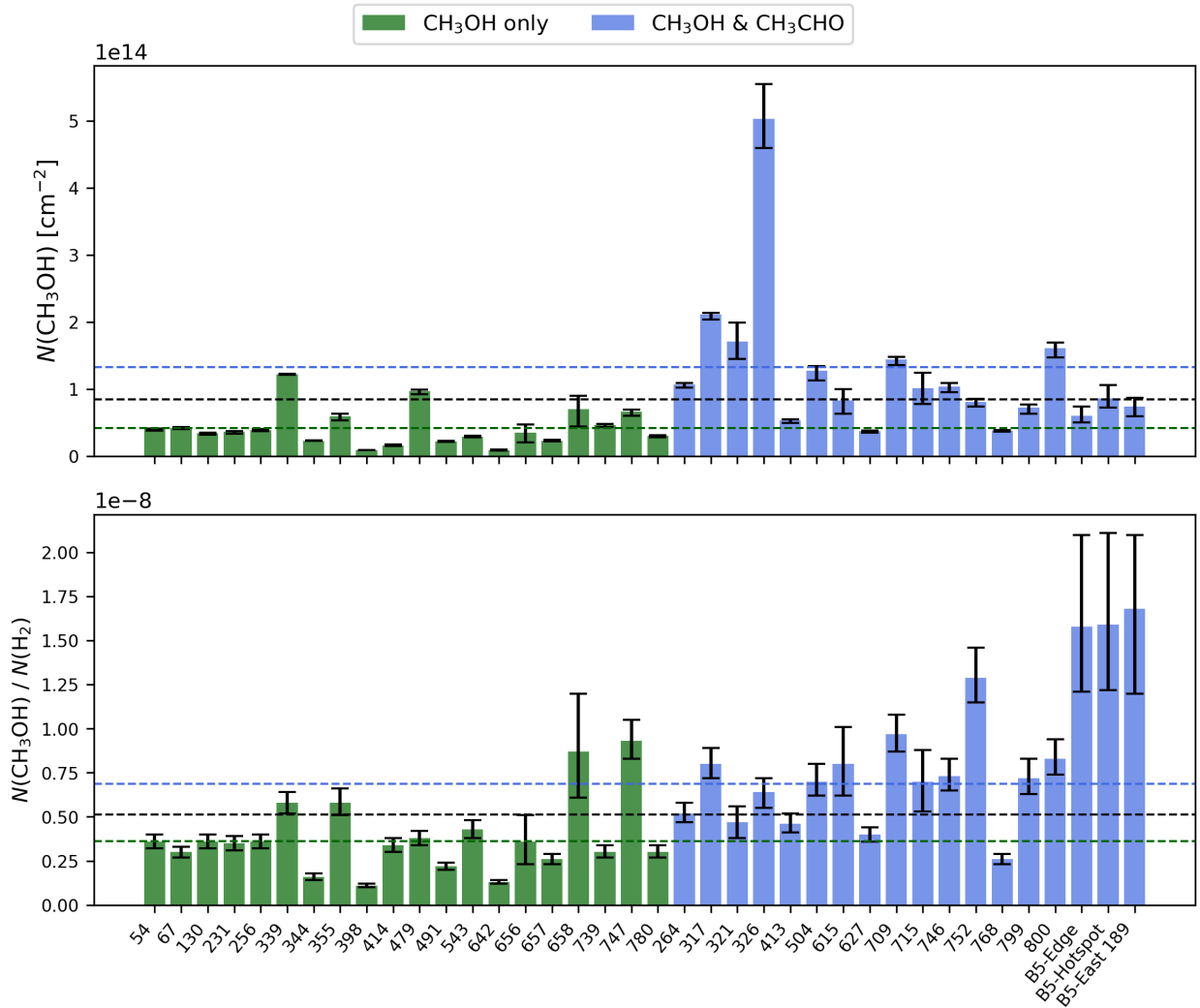


**Fig. 3.**  $\text{CH}_3\text{OH}$  column densities (top panel) and abundances with respect to  $\text{H}_2$  (bottom panel) for a set of starless and prestellar cores in Perseus (Scibelli et al. 2024) compared to B5-Edge, B5-Hotspot, and B5-East 189. The green and blue bars indicate respectively sources without and with an additional detection of  $\text{CH}_3\text{CHO}$ . The horizontal dashed green and blue lines mark the mean values for the two source sets and the dashed black line marks the total mean of all sources (excluding our target sources in all cases).

molecule is formed from the other (however, see also Belloche et al. 2020).  $\text{CH}_3\text{OCHO}$  and  $\text{CH}_3\text{OCH}_3$  do share the common precursor radical  $\text{CH}_3\text{O}^*$  through the proposed surface reactions



It is furthermore speculated that  $\text{CH}_3\text{OCHO}$  might form indirectly from  $\text{CH}_3\text{OCH}_3$  via gas phase reactions (9) and (10). Even though there is convincing observational evidence of a relation between  $\text{CH}_3\text{OCHO}$  and  $\text{CH}_3\text{OCH}_3$  for protostellar sources, the relation for cold sources is less well established. In Fig. 5 we compare measured column densities and abundances of  $\text{CH}_3\text{OCHO}$  and  $\text{CH}_3\text{OCH}_3$  (with respect to  $\text{H}_2$ ) for our B5 target positions, the three cores from the Scibelli et al. (2024) Perseus sample with simultaneous detections of both molecules, as well as a couple of other cold molecular cloud sources. We obtain Pearson  $r$ -values of 0.81 and 0.76 for the column density and abundance relations, respectively, indicating a strong positive linear trend. However, uncertainties are not considered in this estimate and we note that the uncertainties get quite high,

especially for abundances with respect to  $\text{H}_2$ . Furthermore, the sample set and the abundance range are relatively small, and the abundance correlation is generally weaker than for protostellar sources where reported  $r$ -values are commonly  $\geq 0.9$  (Bisschop et al. 2007; Jaber et al. 2014) and up to 0.99 (Coletta et al. 2020).

To test the possible relation between  $\text{CH}_2\text{CO}$  and  $\text{CH}_3\text{CHO}$ , in which  $\text{CH}_3\text{CHO}$  forms by hydrogenation of  $\text{CH}_2\text{CO}$ , we plot the  $N(\text{CH}_3\text{CHO})/N(\text{CH}_2\text{CO})$  ratio measured for our target positions, the cores in the Perseus sample, and a number of other cold cores (see Fig. 6). We plot the ratio as a function of  $\text{CH}_3\text{OH}$  column density and find an increase of the ratio that seems to follow a step-like function. The logistic (sigmoid) function that best describes the data points (excluding L183 and neglecting uncertainties) is shown as a black dashed line. The increase of the  $N(\text{CH}_3\text{CHO})/N(\text{CH}_2\text{CO})$  ratio as a function of  $N(\text{CH}_3\text{OH})$  might be interpreted as an indication of the higher chemical complexity of the sources, considering that sources with higher  $N(\text{CH}_3\text{OH})$  tend to have higher abundances of larger COMs. However, we note that only 4/24 plotted sources with high  $N(\text{CH}_3\text{OH})$  actually show a  $N(\text{CH}_3\text{CHO})/N(\text{CH}_2\text{CO})$  ratio  $> 1$ . Two of those four sources belong to the three Perseus

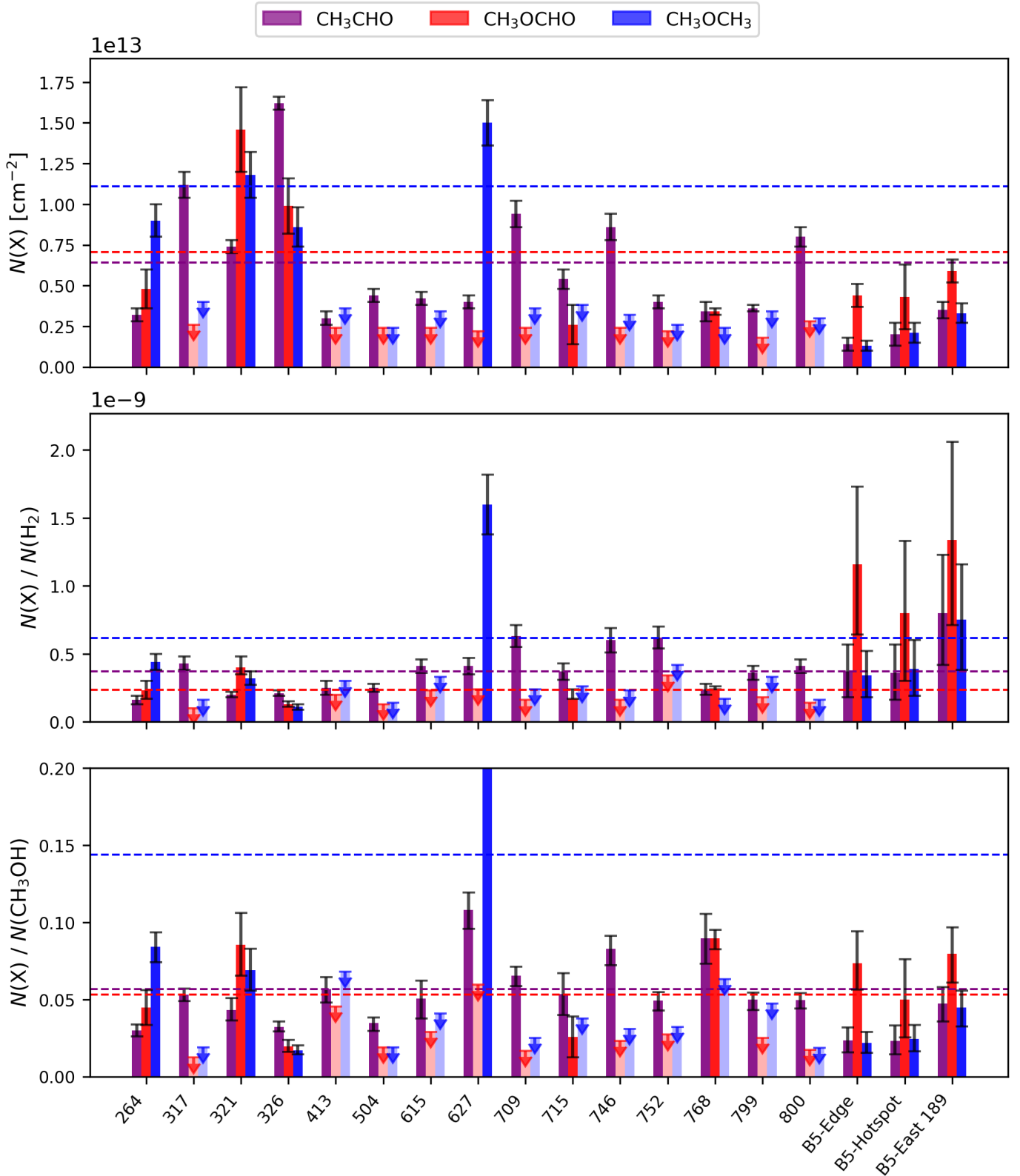


**Fig. 4.** Column densities (top panel), abundances with respect to H<sub>2</sub> (middle panel), and abundances with respect to CH<sub>3</sub>OH (bottom panel) of CH<sub>3</sub>CHO, CH<sub>3</sub>OCHO, and CH<sub>3</sub>OCH<sub>3</sub> for a set of starless and prestellar cores in Perseus (Scibelli et al. 2024) compared to B5-Edge, B5-Hotspot, and B5-East 189. Shown are only those 15 sources of the Perseus sample in which at least CH<sub>3</sub>CHO is detected along with CH<sub>3</sub>OH. The transparent bars indicate upper limits, and the horizontal dashed purple, red, and blue lines mark the mean values for CH<sub>3</sub>CHO, CH<sub>3</sub>OCHO, and CH<sub>3</sub>OCH<sub>3</sub>, respectively (excluding our target sources). The CH<sub>3</sub>OCH<sub>3</sub> abundance of core 627 with respect to CH<sub>3</sub>OH is  $\sim 0.4$ , but we truncated at 0.2 for better visibility.

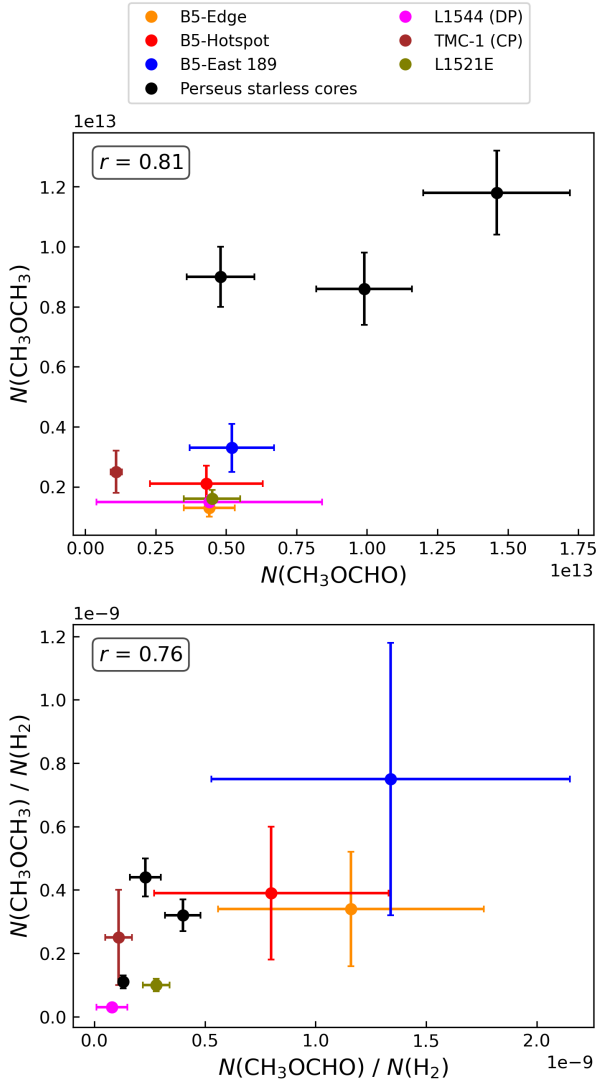


**Fig. 5.** Relation between the column densities (top panel) and abundances with respect to  $H_2$  (bottom panel) of  $CH_3OCHO$  and  $CH_3OCH_3$ . Shown are the values for the B5 positions, a set of starless and prestellar cores in Perseus (Scibelli et al. 2024, only cores with simultaneous detections of both molecules), as well as for the dust peak of L1544 (Jiménez-Serra et al. 2016), the cyanopolyne peak in TMC-1 (Gratier et al. 2016), and L1521E (Scibelli et al. 2021). The Pearson  $r$ -value for the data is given in the upper left corner of each panel.

cores with simultaneous detections of  $CH_3CHO$ ,  $CH_3OCHO$ , and  $CH_3OCH_3$  located in the active region NGC1333, i.e., cores 321 and 326. In the third of these cores, i.e., core 264,  $CH_2CO$  is not detected, which might indicate a well-advanced conversion of  $CH_2CO$  to  $CH_3CHO$ . The remaining sources with lower  $N(CH_3OH)$  show similar ratios around 0.3–0.5, with some sources at the lowest  $N(CH_3OH)$ , i.e., cores 4149 and 1390, and TMC-1 (CP), having slightly elevated  $N(CH_3CHO)/N(CH_2CO)$  ratios, while the ratio of L183 is highly elevated and appears to be an outlier. A reason for this might be that L183 is a chemically evolved core with high abundances of O-rich COMs and low abundances of C-rich COMs such as  $CH_2CO$  (Lattanzi et al. 2020). Therefore, the high  $N(CH_3CHO)/N(CH_2CO)$  ratio for L183 might be an expression of the progressed conversion of  $CH_2CO$  to  $CH_3CHO$ . We also note that even though the prestellar core L1544 is known to be a highly evolved, chemically complex source, it appears in the lower left corner of this plot.

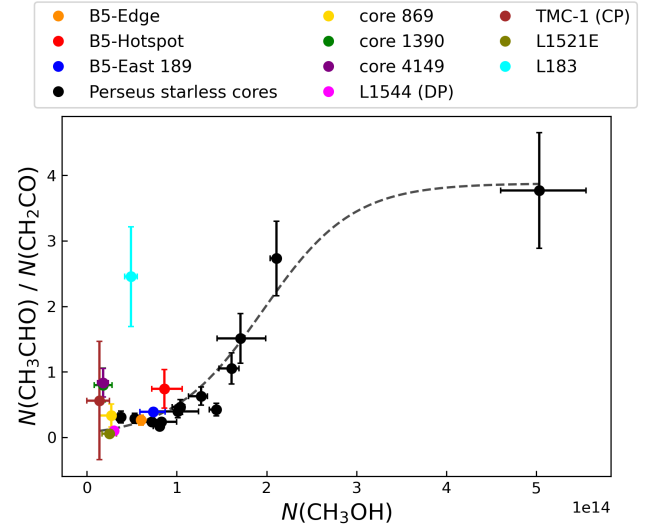


**Fig. 6.**  $N(CH_3CHO)/N(CH_2CO)$  ratio as a function of  $CH_3OH$  column density for the B5 positions; a set of starless and prestellar cores in Perseus (Scibelli et al. 2024); cold cores 860, 1390, and 4149 (Zhou et al. 2022); the dust peak of L1544 (Vastel et al. 2014); the cyanopolyne peak in TMC-1 (Gratier et al. 2016); L1521E (Nagy et al. 2019); and L183 (Lattanzi et al. 2020). The black dashed line marks the logistic function that best fits the data, excluding L183.

This might be explained by the high density of the L1544 dust peak and the very high degree of freeze-out close to the core center, as observed in Caselli et al. (2022). When interpreting Fig. 6, it is also important to consider the chemical differences between different molecular clouds because, for example, cores in Perseus have on average five times higher  $N(CH_3OH)$  than cores in Taurus (see Sect. 4.3). However, most of the plotted sources, i.e., our B5 sources and the cores of the Scibelli et al. (2024) sample, are located in Perseus and, from this perspective, can be directly compared to each other.

## 5. Conclusions

In order to set observational constraints on the efficient release of ices at B5-Hotspot and on the formation pathways of COMs, we made pointed observations with the IRAM 30 m and OSO 20 m telescopes toward two positions close to B5-Hotspot, i.e., B5-Edge and B5-East 189. The main conclusions are as follows:

- Emission from all targeted COMs, i.e.,  $HCOOH$ ,  $CH_2CO$ ,  $CH_3CHO$ ,  $CH_3OCHO$ ,  $CH_3OCH_3$ , is detected toward B5-Edge and B5-East 189, thus revealing that COMs are extended in the area around B5-Hotspot, and especially toward B5-East 189 in the northeast. Physical conditions and COM abundances with respect to  $H_2$  and  $CH_3OH$  do not differ significantly among the three positions, indicating that the efficient release of ices is not confined to B5-Hotspot, but is also active at B5-Edge and B5-East 189; the three positions likely share a similar physical and chemical evolution. Higher resolution observations would help to better disentangle potential differences in physical conditions. Furthermore, ice observations toward the B5-Hotspot region would be valuable to better constrain the desorption and chemical evolution;
- Physical source parameters, i.e.,  $T_k$  and  $n(H_2)$ , are derived from non-LTE radiative transfer models for methanol. Utilizing a new set of collisional rate coefficients reported in D2024 yields 2–3 times higher  $T_k$  and 10–20 times lower

$n(\text{H}_2)$  compared to using the RF2010 rate coefficients. Future non-LTE methanol excitation analyses should consider these differences, and care should be taken in comparisons and interpretations of those in the literature;

- Evidence of gas kinetic temperatures of  $\sim 20$  K for our target positions (higher than the dust temperature of  $\sim 13$  K) might be a relic of a past grain heating event that released ices in the B5-Hotspot area. A subsequent freeze-out of molecules back onto grains would lead to unusually high  $\text{H}_2\text{O}$  abundances in the top ice monolayers, which could speed up the subsequent surface formation of  $\text{H}_2\text{CO}$  and  $\text{CH}_3\text{OH}$ ;
- Comparisons between the COM data of this study and COM data for starless and prestellar cores in Perseus indicate that ices in the B5-Hotspot region might be less evolved but released more efficiently. In addition, gas phase abundances of  $\text{CH}_3\text{OCHO}$  that are systematically higher than the average of cold cores in Perseus and higher than the  $\text{CH}_3\text{OCH}_3$  abundances might indicate efficient gas phase conversion of  $\text{CH}_3\text{OCH}_3$  to  $\text{CH}_3\text{OCHO}$  in the B5-Hotspot region;
- Considering the  $\text{CH}_3\text{OCHO}$  and  $\text{CH}_3\text{OCH}_3$  data of this study and other literature data supports a relation between both molecules for cold molecular cloud sources, similar to the case of protostellar sources, discussed in many places in the literature. Furthermore, considering the  $\text{CH}_2\text{CO}$  and  $\text{CH}_3\text{CHO}$  data of this study and other data from the literature supports the surface formation of  $\text{CH}_3\text{CHO}$  by hydrogenation of  $\text{CH}_2\text{CO}$  at low temperatures.

**Acknowledgements.** The authors acknowledge support from the Institut de Radioastronomie Millimétrique (IRAM) and the Onsala Space Observatory (OSO) for the provisioning of their facilities/observational support. The OSO national research infrastructure is funded through Swedish Research Council grant No. 2017-00648. This work was supported by Chalmers Gender Initiative for Excellence (Genie). The work of SBC was supported by the Goddard Center for Astrobiology and by the NASA Planetary Science Division Internal Scientist Funding Program through the Fundamental Laboratory Research (FLaRe) work package. This research has made use of data from the Herschel Gould Belt survey (HGBS) project (<http://gouldbelt-herschel.cea.fr>). The HGBS is a Herschel Key Program jointly carried out by SPIRE Specialist Astronomy Group 3 (SAG 3), scientists of several institutes in the PACS Consortium (CEA Saclay, INAF-IFSI Rome and INAF-Arcetri, KU Leuven, MPIA Heidelberg), and scientists of the Herschel Science Center (HSC). We are grateful to the IRAM 30 m AoD who acquired B5-Edge data during the IRAM pool week in winter 2024, to John Black for discussion of methanol collisional rate coefficients, and to the anonymous referee whose comments were of great help in improving the quality of this work.

## References

- Agúndez, M., Cernicharo, J., & Guélin, M. 2015, *A&A*, 577, L5
- André, P., Men'shchikov, A., Bontemps, S., et al. 2010, *A&A*, 518, L102
- Bacmann, A., & Faure, A. 2016, *A&A*, 587, A130
- Bacmann, A., Taquet, V., Faure, A., Kahane, C., & Ceccarelli, C. 2012, *A&A*, 541, L12
- Balucani, N., Ceccarelli, C., & Taquet, V. 2015, *MNRAS*, 449, L16
- Belloche, A., Maury, A. J., Maret, S., et al. 2020, *A&A*, 635, A198
- Bernstein, M. P., Dworkin, J. P., Sandford, S. A., Cooper, G. W., & Allamandola, L. J. 2002, *Nature*, 416, 401
- Bisschop, S. E., Jørgensen, J. K., van Dishoeck, E. F., & de Wachter, E. B. M. 2007, *A&A*, 465, 913
- Boogert, A. C. A., Pontoppidan, K. M., Knez, C., et al. 2008, *ApJ*, 678, 985
- Boogert, A. C. A., Huard, T. L., Cook, A. M., et al. 2011, *ApJ*, 729, 92
- Boogert, A. C. A., Gerakines, P. A., & Whittet, D. C. B. 2015, *ARA&A*, 53, 541
- Borsicheva, K., Fedoseev, G., Punanova, A. F., et al. 2025, *ApJ*, 990, 163
- Carl, T., Wirstrom, E. S., Bergman, P., et al. 2023, *MNRAS*, 524, 5993
- Caselli, P., Keto, E., Bergin, E. A., et al. 2012, *ApJ*, 759, L37
- Caselli, P., Pineda, J. E., Sipilä, O., et al. 2022, *ApJ*, 929, 13
- Cernicharo, J., Marcelino, N., Roueff, E., et al. 2012, *ApJ*, 759, L43
- Chiar, J. E., Pendleton, Y. J., Allamandola, L. J., et al. 2011, *ApJ*, 731, 9
- Chu, L. E. U., Hodapp, K., & Boogert, A. 2020, *ApJ*, 904, 86
- Chuang, K.-J., Fedoseev, G., Qasim, D., et al. 2018, *ApJ*, 853, 102
- Coletta, A., Fontani, F., Rivilla, V. M., et al. 2020, *A&A*, 641, A54
- Cuppen, H., Penteado, E., Isokoski, K., van der Marel, N., & Linnartz, H. 2011, *MNRAS*, 417, 2809
- Dagdigian, P. J. 2024, *MNRAS*, 527, 2209
- Dubernet, M., Boursier, C., Denis-Alpizar, O., et al. 2024, *A&A*, 683, A40
- Fabricant, B., Krieger, D., & Muentzer, J. 1977, *J. Chem. Phys.*, 67, 1576
- Friberg, P., Madden, S. C., Hjalmarson, A., & Irvine, W. M. 1988, *A&A*, 195, 281
- Fuchs, G. W., Cuppen, H. M., Ioppolo, S., et al. 2009, *A&A*, 505, 629
- García de la Concepción, J., Colzi, L., Jiménez-Serra, I., et al. 2022, *A&A*, 658, A150
- Garrod, R. T., Jin, M., Matis, K. A., et al. 2022, *ApJS*, 259, 1
- Goto, M., Vasyunin, A. I., Giuliano, B. M., et al. 2021, *A&A*, 651, A53
- Gratier, P., Majumdar, L., Ohishi, M., et al. 2016, *ApJS*, 225, 25
- Hamberg, M., Geppert, W. D., Thomas, R. D., et al. 2007, *Mol. Phys.*, 105, 899
- Hiraoka, K., Ohashi, N., Kihara, Y., et al. 1994, *Chem. Phys. Lett.*, 229, 408
- Huang, K. Y., Behrens, E., Bouvier, M., et al. 2025, *A&A*, 699, A70
- Ilyushin, V., Kryvda, A., & Alekseev, E. 2009, *J. Mol. Spectrosc.*, 255, 32
- Ioppolo, S., Fedoseev, G., Chuang, K.-J., et al. 2021, *Nat. Astron.*, 5, 197
- Jaber, A. A., Ceccarelli, C., Kahane, C., & Caux, E. 2014, *ApJ*, 791, 29
- Jiménez-Serra, I., Vasyunin, A. I., Caselli, P., et al. 2016, *ApJ*, 830, L6
- Jin, M., & Garrod, R. 2020, *ApJS*, 249, 26
- Justtanont, K., Bergman, P., Larsson, B., et al. 2005, *A&A*, 439, 627
- Kalvans, J., & Silsbee, K. 2022, *MNRAS*, 515, 785
- Klapper, G., Lewen, F., Gendriesch, R., Belov, S. P., & Winnewisser, G. 2001, *Z. Naturforsch. A*, 56, 329
- Kleiner, I., Lovas, F. J., & Godefroid, M. 1996, *J. Phys. Chem. Ref. Data*, 25, 1113
- Lacy, J. H., Knacke, R., Geballe, T. R., & Tokunaga, A. T. 1994, *ApJ*, 428, L69
- Lampton, M., Margon, B., & Bowyer, S. 1976, *ApJ*, 208, 177
- Lattanzi, V., Bizzocchi, L., Vasyunin, A. I., et al. 2020, *A&A*, 633, A118
- Lovas, F., Lutz, H., & Dreizler, H. 1979, *J. Phys. Chem. Ref. Data*, 8, 1051
- Maercker, M., Schöier, F. L., Olofsson, H., Bergman, P., & Ramstedt, S. 2008, *A&A*, 479, 779
- Mathews, H. E., Friberg, P., & Irvine, W. M. 1985, *ApJ*, 290, 609
- McClure, M. K., Rocha, W. R. M., Pontoppidan, K. M., et al. 2023, *Nat. Astron.*, 7, 431
- Müller, H. S. P., Schlöder, F., Stutzki, J., & Winnewisser, G. 2005, *J. Mol. Struct.*, 742, 215
- Müller, B., Giuliano, B., Goto, M., & Caselli, P. 2021, *A&A*, 652, A126
- Nagy, Z., Spezzano, S., Caselli, P., et al. 2019, *A&A*, 630, A136
- Nuevo, M., Cooper, G., & Sandford, S. A. 2018, *Nat. Commun.*, 9, 5276
- Nummelin, A., Dickens, J. E., Bergman, P., et al. 1998, *A&A*, 337, 275
- Ohishi, M., Kawaguchi, K., Kaifu, N., et al. 1991, *ASP Conf. Ser.*, 16, 387
- Penteado, E., Boogert, A., Pontoppidan, K., et al. 2015, *MNRAS*, 454, 531
- Pickett, H. M., Poynter, R. L., Cohen, E. A., et al. 1998, *J. Quant. Spect. Radiat. Transf.*, 60, 883
- Pirim, C., & Krim, L. 2011, *Chem. Phys.*, 380, 67
- Priestley, F. D., Clark, P. C., Ragan, S. E., et al. 2025, *MNRAS*, 537, 2453
- Punanova, A., Vasyunin, A., Caselli, P., et al. 2022, *ApJ*, 927, 213
- Rabli, D., & Flower, D. R. 2010, *MNRAS*, 406, 95
- Rivilla, V. M., Beltrán, M. T., Cesaroni, R., et al. 2017, *A&A*, 598, A59
- Roy, A., André, P., Palmeirim, P., et al. 2014, *A&A*, 562, A138
- Rybicki, G. B., & Hummer, D. G. 1991, *A&A*, 245, 171
- Sadavoy, S. 2013, PhD thesis, University of Victoria, Canada
- Saito, S. 1972, *ApJ*, 178, L95
- Scibelli, S., & Shirley, Y. 2020, *ApJ*, 891, 73
- Scibelli, S., Shirley, Y., Vasyunin, A., & Launhardt, R. 2021, *MNRAS*, 504, 5754
- Scibelli, S., Shirley, Y., Megías, A., & Jiménez-Serra, I. 2024, *MNRAS*, 533, 4104
- Skouteris, D., Balucani, N., Ceccarelli, C., et al. 2018, *ApJ*, 854, 135
- Taquet, V., Wirstrom, E. S., Charnley, S. B., et al. 2017, *A&A*, 607, A20
- Tielens, A. G. G. M., Tokunaga, A. T., Geballe, T. R., & Baas, F. 1991, *ApJ*, 381, 181
- Vastel, C., Ceccarelli, C., Lefloch, B., & Bachiller, R. 2014, *ApJ*, 795, L2
- Vasyunin, A., & Herbst, E. 2013, *ApJ*, 769, 34
- Vasyunin, A. I., Caselli, P., Dulieu, F., & Jiménez-Serra, I. 2017, *ApJ*, 842, 33
- Walker, G. W., Kalinauskaitė, E., McCarthy, D. N., et al. 2016, *SpIE*, 9914, 99142V
- Whittet, D. C. B., Shenoy, S. S., Bergin, E. A., et al. 2007, *ApJ*, 655, 332
- Wilson, T. L. 1999, *Rep. Prog. Phys.*, 62, 143
- Winnewisser, M., Winnewisser, B. P., Stein, M., et al. 2002, *J. Mol. Spectrosc.*, 216, 259
- Wirstrom, E. S., Charnley, S. B., Persson, C. M., et al. 2014, *ApJ*, 788, L32
- Xu, L.-H., & Lovas, F. 1997, *J. Phys. Chem. Ref. Data*, 26, 17
- Yang, Y.-L., Sakai, N., Zhang, Y., et al. 2021, *ApJ*, 910, 20
- Zhou, C., Vastel, C., Montillaud, J., et al. 2022, *A&A*, 658, A131
- Zucker, C., Schlafly, E. F., Speagle, J. S., et al. 2018, *ApJ*, 869, 83

## Appendix A: Uncertainties of non-LTE modeling parameters

Uncertainties of  $H_2$  density  $n(H_2)$ , methanol column density  $N(CH_3OH)$ , and kinetic temperature  $T_k$  are derived from  $\chi_{\text{red}}^2$  distribution plots. The methanol column density is calculated as an average over the spherical cloud, according to

$$N(CH_3OH) = \frac{4}{3}Rn(H_2)X(CH_3OH), \quad (\text{A.1})$$

where  $X(CH_3OH)$  is the abundance of methanol with respect to  $H_2$ , which is assumed to be constant. The reduced  $\chi^2$  values are furthermore calculated as

$$\chi_{\text{red}}^2 = \frac{\chi^2}{n}, \quad (\text{A.2})$$

where  $n = x - p$  is the number of degrees of freedom, with  $x$  being the number of considered methanol transitions and  $p$  being the number of simultaneously varied model parameters (2). Plotting values of  $\chi_{\text{red}}^2$  for the sampled values of  $n(H_2)$ ,  $N(CH_3OH)$ , and  $T_k$  gives separate plane sections in the 3D parameter space. In each plane, we identify the position of the local  $\chi_{\text{red}}^2$  minimum and define the (reduced)  $1\sigma$  contour in each plane as the set of points

$$\sigma_{\text{red}} = \min(\chi_{\text{red}}^2)_{\text{glob}} + \frac{3.5}{n}, \quad (\text{A.3})$$

where  $\min(\chi_{\text{red}}^2)_{\text{glob}}$  is the global  $\chi_{\text{red}}^2$  minimum (Lampton et al. 1976). The complete  $1\sigma$  contour has the shape of an ellipsoid, while each elliptical  $1\sigma$  contour results from  $n(H_2)$ - $N(CH_3OH)$  planes cutting through this ellipsoid at a certain  $T_k$ . To determine the uncertainties in  $n(H_2)$ ,  $N(CH_3OH)$ , and  $T_k$ , we identify the four points in the total sampled set  $\sigma_{\text{red}}$  that are farthest away from the global  $\chi_{\text{red}}^2$  minimum. The difference between the parameter values at these four points and the parameter values at the global minimum give the positive and negative uncertainties associated with the parameters.

## Appendix B: Beam convolution for $H_2$ and $CH_3OH$ column densities

Assuming constant values of  $H_2$  density  $n(H_2)$  and methanol abundance  $X(CH_3OH)$ , the beam average column densities of  $H_2$  and  $CH_3OH$  are calculated numerically as

$$N(H_2) = n(H_2) \sum_i L(\mathbf{r}_i)g(\mathbf{r}_i) \Delta r \quad (\text{B.1})$$

and

$$N(CH_3OH) = n(H_2)X(CH_3OH) \sum_i L(\mathbf{r}_i)g(\mathbf{r}_i) \Delta r, \quad (\text{B.2})$$

respectively.  $L(\mathbf{r}) = L(x, y)$  is the position dependent path length (chord length) through the spherical model cloud,  $g(\mathbf{r})$  is the 2D Gaussian beam shape function, and  $\Delta r = \Delta x \Delta y$ . The chord length at a given position  $\mathbf{r}$  is given by

$$L(\mathbf{r}) = 2\sqrt{R^2 - d(\mathbf{r})^2}, \quad (\text{B.3})$$

where  $d(\mathbf{r}) = \sqrt{x^2 + y^2}$  is the distance of  $\mathbf{r}$  from the origin. The beam shape function can be furthermore written in matrix notation as

$$g(\mathbf{r}) = \frac{1}{2\pi} \det(\Sigma)^{-1/2} \exp\left[-\frac{1}{2}(\mathbf{r} - \mathbf{r}_0 | \Sigma^{-1} | \mathbf{r} - \mathbf{r}_0)\right], \quad (\text{B.4})$$

where  $\mathbf{r}_0$  is the assumed beam center, and

$$\Sigma = \begin{pmatrix} \sigma_x^2 & 0 \\ 0 & \sigma_y^2 \end{pmatrix} \quad (\text{B.5})$$

is the covariance matrix, including the Gaussian standard deviations  $\sigma_x$  and  $\sigma_y$ , which, for a circular beam, can be expressed in terms of the half power beam width  $\theta$  as

$$\sigma_x = \sigma_y = \frac{\theta}{2\sqrt{2\ln 2}}. \quad (\text{B.6})$$

Based on the distance  $D$  to the model source (in cm), the sky solid angle covered by the beam is converted from arcsec to centimeter via

$$\theta_{\text{cm}} \approx \frac{D_{\text{cm}}\theta_{\text{arcsec}}}{206265}. \quad (\text{B.7})$$

Fig. D.4 shows the beam convolution for B5-Hotspot and B5-East 189 in the top row, and for B5-Edge in the bottom row. Values of  $L(x, y)$  are calculated from Eq. (B.3), assuming a model cloud radius  $R = 2 \times 10^{17}$  cm, and values of  $g(x, y)$  are calculated from Eq. (B.4), assuming  $D = 302$  pc (Zucker et al. 2018) and  $\theta_{\text{arcsec}} = 38''$ , i.e., the approximate beam size of the OSO 20 m telescope at the strong  $\sim 96.7$  GHz  $CH_3OH(2-1)$  lines. Values for  $N(H_2)$  and  $N(CH_3OH)$  are then calculated from Eqs. (B.1) and (B.2), respectively, using the best fit values of  $n(H_2)$  and  $X(CH_3OH)$  for B5-Hotspot and B5-East 189. In case of B5-Edge, we use the best fit parameters for B5-Hotspot, while the beam center is shifted from  $\mathbf{r}_0 = (0, 0)$  to  $\mathbf{r}_0 = (0.6R, 0)$ . The uncertainties of the beam average column densities of  $H_2$  and  $CH_3OH$  are furthermore calculated from the uncertainties estimated for  $n(H_2)$  and  $N(CH_3OH)$  in the previous section. In that section,  $N(CH_3OH)$  was calculated more approximate via Eq. (A.1). However, the relative uncertainty associated with the column density does not change even though the way of calculating the column density is changed.

## Appendix C: LTE column density calculation

Assuming optically thin emission and local thermal/thermodynamic equilibrium (LTE) conditions, the column density  $N$  of a molecule X is given as

$$N(X) = \frac{1}{C} \int T_{\text{mb}} dv, \quad (\text{C.1})$$

where  $\int T_{\text{mb}} dv$  is the integrated intensity and  $C$  is a constant, i.e.,

$$C = \frac{hc^3}{8\pi k_B} \frac{g_u A_{ul}}{\nu^2} \frac{\exp(-E_u/T_{\text{ex}})}{Q_{\text{rot}}(T_{\text{ex}})} \left[ 1 - \frac{J_\nu(T_{\text{bg}})}{J_\nu(T_{\text{ex}})} \right]. \quad (\text{C.2})$$

$h$  is the Planck constant,  $c$  is the speed of light,  $k_B$  is the Boltzmann constant,  $T_{\text{ex}}$  is the excitation temperature,  $T_{\text{bg}} \approx 2.725$  K is the (cosmic microwave) background temperature,  $g_u$  is the total degeneracy,  $A_{ul}$  is the Einstein coefficient of spontaneous emission,  $\nu$  is the transition (rest) frequency,  $E_u$  is the upper level energy (in Kelvin), and  $Q_{\text{rot}}(T)$  is the rotational partition function. Furthermore,  $J_\nu(T)$  is the temperature equivalent of specific intensity, given as

$$J_\nu(T) = \frac{h\nu}{k_B} \left[ \exp\left(\frac{h\nu}{k_B T}\right) - 1 \right]^{-1}. \quad (\text{C.3})$$

The last term in Eq. (C.2) is only needed if  $T_{\text{ex}}$  is comparable to  $T_{\text{bg}}$ , which is the case for the three positions considered in this study.

## Appendix D: Additional tables and figures

Table D.1: Targeted transitions and their spectroscopic properties.

Molecule	Transition	$\nu$ [GHz]	$E_u$ [K]	$A_{ul}$ [s <sup>-1</sup> ]	$g_u$	$Q_{\text{rot}}$ (9.375 K)	$\theta_{\text{HPBW}}$ [arcsec]	Tel. <sup>(a)</sup>	Ref. <sup>(b)</sup>
C <sup>18</sup> O	1 – 0	109.78217	5.3	$6.3 \times 10^{-8}$	3	3.9	33.7	O20	(1)
HCO*	1 <sub>0,1</sub> – 0 <sub>0,0</sub> , $F = 2 - 1$	86.67076	4.2	$4.7 \times 10^{-6}$	5	20.3	28.5	I30	(2)
HCO*	1 <sub>0,1</sub> – 0 <sub>0,0</sub> , $F = 1 - 0$	86.70836	4.2	$4.6 \times 10^{-6}$	3	20.3	28.5	I30	
HCO*	1 <sub>0,1</sub> – 0 <sub>0,0</sub> , $F = 1 - 1$	86.77746	4.2	$4.6 \times 10^{-6}$	3	20.3	28.4	I30	
HCO*	1 <sub>0,1</sub> – 0 <sub>0,0</sub> , $F = 0 - 1$	86.80578	4.2	$4.7 \times 10^{-6}$	1	20.3	28.4	I30	
<i>t</i> -HCOOH	4 <sub>1,4</sub> – 3 <sub>1,3</sub>	86.54619	13.6	$6.4 \times 10^{-6}$	9	49.9	28.5	I30	(3)
<i>c</i> -HCOOH	4 <sub>0,4</sub> – 3 <sub>0,3</sub>	87.69469	10.5	$2.5 \times 10^{-5}$	9	48.3	28.1	I30	
<i>o</i> -CH <sub>2</sub> CO	5 <sub>1,5</sub> – 4 <sub>1,4</sub>	100.09451	27.5	$1.0 \times 10^{-5}$	33	47.6	24.6	I30	(4)
E-CH <sub>3</sub> OH	5 <sub>-1</sub> – 4 <sub>0</sub>	84.52117	40.4	$2.0 \times 10^{-6}$	11	19.5	29.2	I30	(5)
A <sup>+</sup> -CH <sub>3</sub> OH	2 <sub>1</sub> – 1 <sub>1</sub>	95.91431	21.4	$2.5 \times 10^{-6}$	5	19.5	38.6	O20	
E-CH <sub>3</sub> OH	2 <sub>-1</sub> – 1 <sub>-1</sub>	96.73936	12.5	$2.6 \times 10^{-6}$	5	19.5	38.3	O20	
A <sup>+</sup> -CH <sub>3</sub> OH	2 <sub>0</sub> – 1 <sub>0</sub>	96.74137	7.0	$3.4 \times 10^{-6}$	5	19.5	38.3	O20	
E-CH <sub>3</sub> OH	2 <sub>0</sub> – 1 <sub>0</sub>	96.74455	20.1	$3.4 \times 10^{-6}$	5	19.5	38.2	O20	
E-CH <sub>3</sub> OH	2 <sub>1</sub> – 1 <sub>1</sub>	96.75550	28.0	$2.6 \times 10^{-6}$	5	19.5	38.2	O20	
A <sup>-</sup> -CH <sub>3</sub> OH	2 <sub>1</sub> – 1 <sub>1</sub>	97.58280	21.6	$2.6 \times 10^{-6}$	5	19.5	37.9	O20	
E-CH <sub>3</sub> OH	0 <sub>0</sub> – 1 <sub>-1</sub>	108.89395	13.1	$1.5 \times 10^{-5}$	1	19.5	34.0	O20	
E-CH <sub>3</sub> CHO	2 <sub>1,2</sub> – 1 <sub>0,1</sub>	83.58428	5.0	$2.2 \times 10^{-6}$	5 <sup>(c)</sup>	132 <sup>(d)</sup>	29.5	I30	(6)
A-CH <sub>3</sub> CHO	2 <sub>1,2</sub> – 1 <sub>0,1</sub>	84.21975	5.0	$2.4 \times 10^{-6}$	5 <sup>(c)</sup>	132 <sup>(d)</sup>	29.3	I30	
E-CH <sub>3</sub> CHO	5 <sub>1,5</sub> – 4 <sub>1,3</sub>	98.86331	16.6	$3.1 \times 10^{-5}$	11 <sup>(c)</sup>	132 <sup>(d)</sup>	25.0	I30	
A-CH <sub>3</sub> CHO	5 <sub>1,5</sub> – 4 <sub>1,3</sub>	98.90094	16.5	$3.1 \times 10^{-5}$	11 <sup>(c)</sup>	132 <sup>(d)</sup>	24.9	I30	
E-CH <sub>3</sub> OCHO	7 <sub>2,6</sub> – 6 <sub>2,5</sub>	84.44917	19.0	$8.0 \times 10^{-6}$	30	720.8	29.2	I30	(7)
A-CH <sub>3</sub> OCHO	7 <sub>2,6</sub> – 6 <sub>2,5</sub>	84.45475	19.0	$8.0 \times 10^{-6}$	30	720.8	29.2	I30	
E-CH <sub>3</sub> OCHO	7 <sub>3,4</sub> – 6 <sub>3,3</sub>	87.14328	22.6	$7.8 \times 10^{-6}$	30	720.8	28.3	I30	
A-CH <sub>3</sub> OCHO	7 <sub>3,4</sub> – 6 <sub>3,3</sub>	87.16129	22.6	$7.9 \times 10^{-6}$	30	720.8	28.3	I30	
E-CH <sub>3</sub> OCHO	9 <sub>1,9</sub> – 8 <sub>1,8</sub>	100.07861	25.0	$1.5 \times 10^{-5}$	38	720.8	24.6	I30	
A-CH <sub>3</sub> OCHO	9 <sub>1,9</sub> – 8 <sub>1,8</sub>	100.08054	24.9	$1.5 \times 10^{-5}$	38	720.8	24.6	I30	
E-CH <sub>3</sub> OCHO	8 <sub>1,7</sub> – 7 <sub>1,6</sub>	100.48224	22.8	$1.4 \times 10^{-5}$	34	720.8	24.6	I30	
A-CH <sub>3</sub> OCHO	8 <sub>1,7</sub> – 7 <sub>1,6</sub>	100.49068	22.8	$1.4 \times 10^{-5}$	34	720.8	24.5	I30	
E-CH <sub>3</sub> OCHO	8 <sub>2,6</sub> – 7 <sub>2,5</sub>	103.46657	24.6	$1.5 \times 10^{-5}$	34	720.8	23.8	I30	
A-CH <sub>3</sub> OCHO	8 <sub>2,6</sub> – 7 <sub>2,5</sub>	103.47866	24.6	$1.5 \times 10^{-5}$	34	720.8	23.8	I30	
EA-CH <sub>3</sub> OCH <sub>3</sub>	4 <sub>1,4</sub> – 3 <sub>0,3</sub>	99.32443	10.2	$4.4 \times 10^{-6}$	18	1334	24.8	I30	(8)
AE-CH <sub>3</sub> OCH <sub>3</sub>	4 <sub>1,4</sub> – 3 <sub>0,3</sub>	99.32443	10.2	$4.4 \times 10^{-6}$	27	1334	24.8	I30	
EE-CH <sub>3</sub> OCH <sub>3</sub>	4 <sub>1,4</sub> – 3 <sub>0,3</sub>	99.32525	10.2	$4.4 \times 10^{-6}$	72	1334	24.8	I30	
AA-CH <sub>3</sub> OCH <sub>3</sub>	4 <sub>1,4</sub> – 3 <sub>0,3</sub>	99.32600	10.2	$4.4 \times 10^{-6}$	45	1334	24.8	I30	

(a) O20 = OSO 20 m; I30 = IRAM 30 m.

(b) key spectroscopic references: (1) Klapper et al. (2001), (2) Saito (1972), (3) Winnewisser et al. (2002), (4) Fabricant et al. (1977), (5) Xu &amp; Lovas (1997), (6) Kleiner et al. (1996), (7) Ilyushin et al. (2009), (8) Lovas et al. (1979);

- data taken from CDMS (C<sup>18</sup>O, HCOOH) and JPL (remaining molecules);- CDMS: <https://cdms.astro.uni-koeln.de/> (Müller et al. 2005);- JPL: <https://spec.jpl.nasa.gov/> (Pickett et al. 1998).(c) we use  $g_u = 2J + 1$  to be consistent with  $Q_{\text{rot}}(T)$  from Nummelin et al. (1998).(d) from Nummelin et al. (1998) for A-/E-conformers combined, i.e.,  $Q_{\text{rot}}(T) = 4.6 \times T^{3/2}$ .

Table D.2: Measured spectral line parameters.

Molecule	Transition	B5-Edge			B5-East 189			B5-Hotspot		
		FWHM <sup>(a)</sup> (km s <sup>-1</sup> )	$\int T_{\text{mb}} d\nu^{(b)}$ (mK km s <sup>-1</sup> )	RMS <sup>(c)</sup> (mK)	FWHM <sup>(a)</sup> (km s <sup>-1</sup> )	$\int T_{\text{mb}} d\nu^{(b)}$ (mK km s <sup>-1</sup> )	RMS <sup>(c)</sup> (mK)	FWHM <sup>(a)</sup> (km s <sup>-1</sup> )	$\int T_{\text{mb}} d\nu^{(b)}$ (mK km s <sup>-1</sup> )	RMS <sup>(c)</sup> (mK)
C <sup>18</sup> O	1-0	0.72 ± 0.01	2286.8 ± 18.9	23.0	0.70 ± 0.02	2455.3 ± 21.2	26.0	0.70 ± 0.01	2653.5 ± 20.5	25.0
HCO*	F = 2-1	0.70 ± 0.03	40.3 ± 1.2	2.0	0.54 ± 0.02	66.3 ± 2.9	4.5			
HCO*	F = 1-0	0.68 ± 0.03	23.5 ± 1.1	1.8	0.57 ± 0.03	46.8 ± 2.4	3.8			
HCO*	F = 1-1	0.72 ± 0.03	22.1 ± 0.9	1.4	0.51 ± 0.03	40.0 ± 2.5	3.9			
HCO*	F = 0-1	0.67 ± 0.09	8.7 ± 1.3	2.1	0.46 ± 0.08	11.9 ± 2.3	3.6			
<i>t</i> -HCOOH	4 <sub>1,4</sub> - 3 <sub>1,3</sub>	0.68 ± 0.04	21.3 ± 1.1	1.9	0.45 ± 0.05	22.8 ± 2.8	4.7			
<i>c</i> -HCOOH	4 <sub>0,4</sub> - 3 <sub>0,3</sub>	1.05 ± 0.15	9.3 ± 1.0	1.7	0.30 ± 0.09	4.3 ± 2.4	4.1			
<i>o</i> -CH <sub>2</sub> CO	5 <sub>1,5</sub> - 4 <sub>1,4</sub>	0.59 ± 0.03	27.4 ± 1.1	2.1	0.48 ± 0.02	58.6 ± 2.4	4.6			
E-CH <sub>3</sub> OH	5 <sub>-1</sub> - 4 <sub>0</sub>	0.58 ± 0.01	44.8 ± 1.2	1.8	0.52 ± 0.01	72.1 ± 1.9	2.9			
A <sup>+</sup> -CH <sub>3</sub> OH	2 <sub>1</sub> - 1 <sub>1</sub>	< 38.1		17.1		< 37.7	18.2			< 37.1
E-CH <sub>3</sub> OH	2 <sub>-1</sub> - 1 <sub>-1</sub>	0.72 ± 0.03	1077.6 ± 10.6	13.5	0.67 ± 0.04	1225.5 ± 10.9	14.0	0.66 ± 0.02	1401.1 ± 12.5	16.0
A <sup>+</sup> -CH <sub>3</sub> OH	2 <sub>0</sub> - 1 <sub>0</sub>	0.71 ± 0.06	1384.0 ± 10.3	13.1	0.70 ± 0.04	1654.6 ± 11.1	14.2	0.68 ± 0.05	1835.1 ± 10.7	13.6
E-CH <sub>3</sub> OH	2 <sub>0</sub> - 1 <sub>0</sub>	0.64 ± 0.04	165.6 ± 9.6	12.1	0.64 ± 0.04	218.3 ± 13.1	16.5	0.59 ± 0.04	230.5 ± 13.2	16.7
E-CH <sub>3</sub> OH	2 <sub>1</sub> - 1 <sub>1</sub>	< 37.8		17.0		< 28.1	13.6			< 30.7
A <sup>-</sup> -CH <sub>3</sub> OH	2 <sub>1</sub> - 1 <sub>1</sub>	< 31.6		14.2		< 33.0	16.0			< 34.6
E-CH <sub>3</sub> OH	0 <sub>0</sub> - 1 <sub>-1</sub>	0.76 ± 0.06	269.7 ± 18.8	24.7	0.64 ± 0.04	260.5 ± 18.9	24.7	0.60 ± 0.03	327.9 ± 17.7	23.2
E-CH <sub>3</sub> CHO	2 <sub>1,2</sub> - 1 <sub>0,1</sub>	0.57 ± 0.11	6.0 ± 1.1	1.8	0.52 ± 0.10	11.8 ± 2.3	4.0			
A-CH <sub>3</sub> CHO	2 <sub>1,2</sub> - 1 <sub>0,1</sub>	0.70 ± 0.17	5.2 ± 1.2	2.1	0.51 ± 0.09	15.4 ± 2.1	3.5			
E-CH <sub>3</sub> CHO	5 <sub>1,5</sub> - 4 <sub>1,3</sub>	0.59 ± 0.06	11.9 ± 1.1	2.1	0.43 ± 0.04	31.4 ± 3.1	5.7			
A-CH <sub>3</sub> CHO	5 <sub>1,5</sub> - 4 <sub>1,3</sub>	0.44 ± 0.04	14.1 ± 1.1	2.0	0.51 ± 0.05	35.5 ± 3.1	5.6			
E-CH <sub>3</sub> OCHO	7 <sub>2,6</sub> - 6 <sub>2,5</sub>	0.51 ± 0.11	4.4 ± 1.1	1.9	0.45 ± 0.09	12.3 ± 2.5	4.1			
A-CH <sub>3</sub> OCHO	7 <sub>2,6</sub> - 6 <sub>2,5</sub>	< 3.6		1.9	0.43 ± 0.08	9.3 ± 2.1	3.4			
E-CH <sub>3</sub> OCHO	7 <sub>3,4</sub> - 6 <sub>3,3</sub>	< 4.1		2.1		< 7.0	4.4			
A-CH <sub>3</sub> OCHO	7 <sub>3,4</sub> - 6 <sub>3,3</sub>	< 3.1		1.6		< 6.9	4.4			
E-CH <sub>3</sub> OCHO	9 <sub>1,9</sub> - 8 <sub>1,8</sub>	< 4.8		2.5	0.75 ± 0.24	10.9 ± 2.7	5.0			
A-CH <sub>3</sub> OCHO	9 <sub>1,9</sub> - 8 <sub>1,8</sub>	< 4.2		2.2	0.32 ± 0.09	6.9 ± 2.6	5.0			
E-CH <sub>3</sub> OCHO	8 <sub>1,7</sub> - 7 <sub>1,6</sub>	< 4.4		2.3		< 9.9	6.2			
A-CH <sub>3</sub> OCHO	8 <sub>1,7</sub> - 7 <sub>1,6</sub>	< 4.5		2.3	0.57 ± 0.18	5.0 ± 2.8	5.1			
E-CH <sub>3</sub> OCHO	8 <sub>2,6</sub> - 7 <sub>2,5</sub>	< 4.2		2.2		< 8.1	5.1			
A-CH <sub>3</sub> OCHO	8 <sub>2,6</sub> - 7 <sub>2,5</sub>	0.32 ± 0.08	6.6 ± 1.3	2.4	0.44 ± 0.13	10.5 ± 3.1	5.8			
EA/AE-CH <sub>3</sub> OCH <sub>3</sub>	4 <sub>1,4</sub> - 3 <sub>0,3</sub>	< 2.9		1.5		< 6.6	4.2			
EE-CH <sub>3</sub> OCH <sub>3</sub>	4 <sub>1,4</sub> - 3 <sub>0,3</sub>	0.54 ± 0.14	4.6 ± 0.9	1.6	0.39 ± 0.12	10.5 ± 1.9	3.7			
AA-CH <sub>3</sub> OCH <sub>3</sub>	4 <sub>1,4</sub> - 3 <sub>0,3</sub>	< 2.8		1.5	0.65 ± 0.21	10.4 ± 1.9	3.5			

<sup>(a)</sup> derived from Gaussian fits.<sup>(b)</sup> derived by summation over line channels (for C<sup>18</sup>O(1-0)), integrated intensities are calculated from the Gaussian fitting parameters; see section 3.1); uncertainties are derived from the noise.<sup>(c)</sup> calculated in main beam temperature scale over line-free channels in 12 km s<sup>-1</sup> wide spectral windows around the transition frequencies.

Table D.3: Molecular column densities and abundances.

Molecule	$N(X)$ [cm <sup>-2</sup> ]	$N(X)/N(H_2)$	$N(X)/N(CH_3OH)$ [ $\times 10^{-2}$ ]	$N(X)/N(X)_{\text{hotspot}}$	$T_{\text{ex}}$ [K]
B5-Edge					
CH <sub>3</sub> OH	$(6.0^{+1.4}_{-1.0}) \times 10^{13}$	$(1.6^{+0.5}_{-0.4}) \times 10^{-8}$			
C <sup>18</sup> O	$(4.02^{+0.03}_{-0.03}) \times 10^{15}$	$(1.1^{+0.5}_{-0.5}) \times 10^{-6}$			21.0
HCO*	$(7.5^{+0.3}_{-0.3}) \times 10^{11}$	$(2.0^{+0.9}_{-0.8}) \times 10^{-10}$	$1.3^{+0.3}_{-0.2}$		6.5
HCOOH	$(1.79^{+0.09}_{-0.09}) \times 10^{12}$	$(4.7^{+2.3}_{-2.0}) \times 10^{-10}$	$3.0^{+0.7}_{-0.5}$	$0.6 \pm 0.2$	6.5
CH <sub>2</sub> CO	$(5.3^{+0.2}_{-0.2}) \times 10^{12}$	$(13.9^{+6.6}_{-5.9}) \times 10^{-10}$	$8.8^{+2.1}_{-1.5}$	$2.0 \pm 0.3$	6.5
CH <sub>3</sub> CHO	$(1.4^{+0.4}_{-0.4}) \times 10^{12}$	$(3.7^{+2.0}_{-1.9}) \times 10^{-10}$	$2.3^{+0.9}_{-0.8}$	$0.7 \pm 0.3$	5.1
CH <sub>3</sub> OCHO	$(4.4^{+0.7}_{-0.7}) \times 10^{12}$	$(11.6^{+5.7}_{-5.2}) \times 10^{-10}$	$7.3^{+2.0}_{-1.7}$	$1.0 \pm 0.5$	6.5
CH <sub>3</sub> OCH <sub>3</sub>	$(1.3^{+0.3}_{-0.3}) \times 10^{12}$	$(3.4^{+1.8}_{-1.6}) \times 10^{-10}$	$2.2^{+0.7}_{-0.6}$	$0.6 \pm 0.2$	6.5
B5-Hotspot					
CH <sub>3</sub> OH	$(8.6^{+2.0}_{-1.4}) \times 10^{13}$	$(1.6^{+0.5}_{-0.4}) \times 10^{-8}$			
C <sup>18</sup> O	$(4.85^{+0.03}_{-0.03}) \times 10^{15}$	$(9.0^{+4.3}_{-3.8}) \times 10^{-7}$			21.0
HCO*(a)	$(5.7^{+1.5}_{-1.5}) \times 10^{11}$	$(1.1^{+0.6}_{-0.5}) \times 10^{-10}$	$0.7^{+0.2}_{-0.2}$		6.5
HCOOH <sup>(b)</sup>	$(2.8^{+0.7}_{-0.7}) \times 10^{12}$	$(5.2^{+2.8}_{-2.6}) \times 10^{-10}$	$3.3^{+1.1}_{-1.0}$		
CH <sub>2</sub> CO <sup>(b)</sup>	$(2.7^{+0.5}_{-0.5}) \times 10^{12}$	$(5.0^{+2.6}_{-2.3}) \times 10^{-10}$	$3.1^{+0.9}_{-0.7}$		
CH <sub>3</sub> CHO <sup>(c)</sup>	$(2.0^{+0.7}_{-0.7}) \times 10^{12}$	$(3.6^{+2.1}_{-2.0}) \times 10^{-10}$	$2.3^{+0.9}_{-0.8}$		
CH <sub>3</sub> OCHO <sup>(b)</sup>	$(4.3^{+2.0}_{-2.0}) \times 10^{12}$	$(8.0^{+5.3}_{-5.0}) \times 10^{-10}$	$5.0^{+2.6}_{-2.5}$		
CH <sub>3</sub> OCH <sub>3</sub> <sup>(b)</sup>	$(2.1^{+0.6}_{-0.6}) \times 10^{12}$	$(3.9^{+2.1}_{-2.0}) \times 10^{-10}$	$2.4^{+0.9}_{-0.8}$		
B5-East 189					
CH <sub>3</sub> OH	$(7.4^{+1.3}_{-1.5}) \times 10^{13}$	$(1.7^{+0.4}_{-0.5}) \times 10^{-8}$			
C <sup>18</sup> O	$(4.80^{+0.04}_{-0.04}) \times 10^{15}$	$(1.1^{+0.6}_{-0.5}) \times 10^{-6}$			24.0
HCO*	$(13.1^{+0.6}_{-0.6}) \times 10^{11}$	$(3.0^{+1.6}_{-1.4}) \times 10^{-10}$	$1.8^{+0.3}_{-0.4}$		7.0
HCOOH	$(1.7^{+0.2}_{-0.2}) \times 10^{12}$	$(3.9^{+2.1}_{-1.8}) \times 10^{-10}$	$2.3^{+0.5}_{-0.5}$	$0.6 \pm 0.2$	7.0
CH <sub>2</sub> CO	$(9.0^{+0.3}_{-0.3}) \times 10^{12}$	$(20.5^{+10.7}_{-9.3}) \times 10^{-10}$	$12.2^{+2.2}_{-2.5}$	$3.3 \pm 0.6$	7.0
CH <sub>3</sub> CHO	$(3.5^{+0.5}_{-0.5}) \times 10^{12}$	$(8.0^{+4.3}_{-3.8}) \times 10^{-10}$	$4.8^{+1.0}_{-1.2}$	$1.8 \pm 0.6$	5.2
CH <sub>3</sub> OCHO	$(5.9^{+0.7}_{-0.7}) \times 10^{12}$	$(13.4^{+7.2}_{-6.3}) \times 10^{-10}$	$8.0^{+1.7}_{-1.9}$	$1.4 \pm 0.8$	7.0
CH <sub>3</sub> OCH <sub>3</sub>	$(3.3^{+0.6}_{-0.6}) \times 10^{12}$	$(7.5^{+4.1}_{-3.7}) \times 10^{-10}$	$4.5^{+1.1}_{-1.2}$	$1.6 \pm 0.6$	7.0

(a)  $N(\text{HCO}^*)$  calculated from unpublished data obtained with the OSO 20 m telescope (see section 3.3).(b)  $N(\text{HCOOH})$ ,  $N(\text{CH}_2\text{CO})$ ,  $N(\text{CH}_3\text{OCHO})$ , and  $N(\text{CH}_3\text{OCH}_3)$  from Taquet et al. (2017).(c)  $N(\text{CH}_3\text{CHO})$  from Carl et al. (2023).

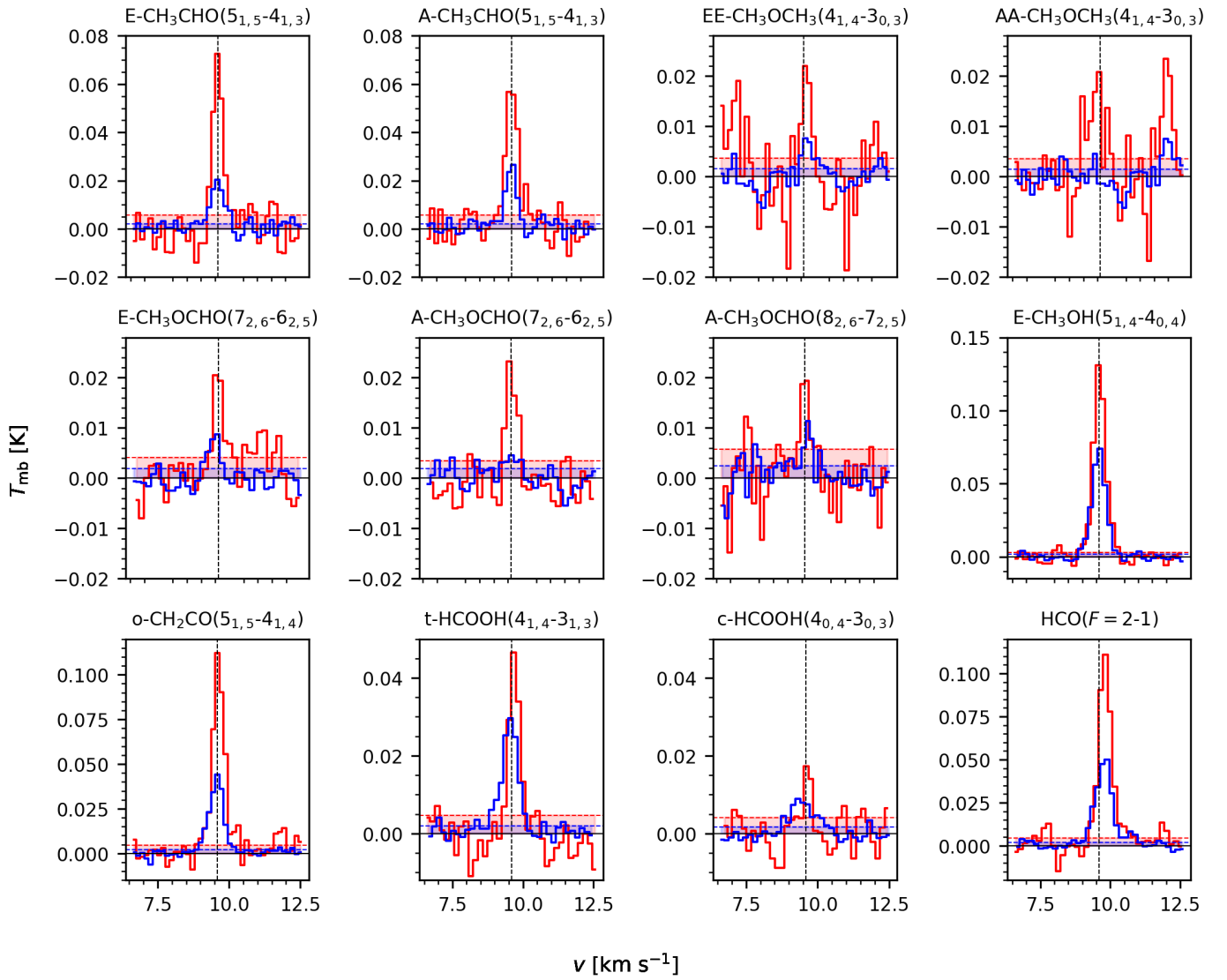


Fig. D.1: Selection of spectral lines detected in the IRAM 30 m data. Top row:  $\text{CH}_3\text{CHO}$  and  $\text{CH}_3\text{OCH}_3$ ; middle row:  $\text{CH}_3\text{OCHO}$  and  $\text{CH}_3\text{OH}$ ; bottom row:  $\text{CH}_2\text{CO}$ ,  $\text{HCOOH}$ , and  $\text{HCO}^+$ . Blue and red indicate B5-Edge and B5-East 189, respectively. The dashed vertical black line marks the assumed source LSR velocity ( $9.6 \text{ km s}^{-1}$ ), and the shaded blue and red areas mark the calculated RMS noise levels as reported in Table D.2.

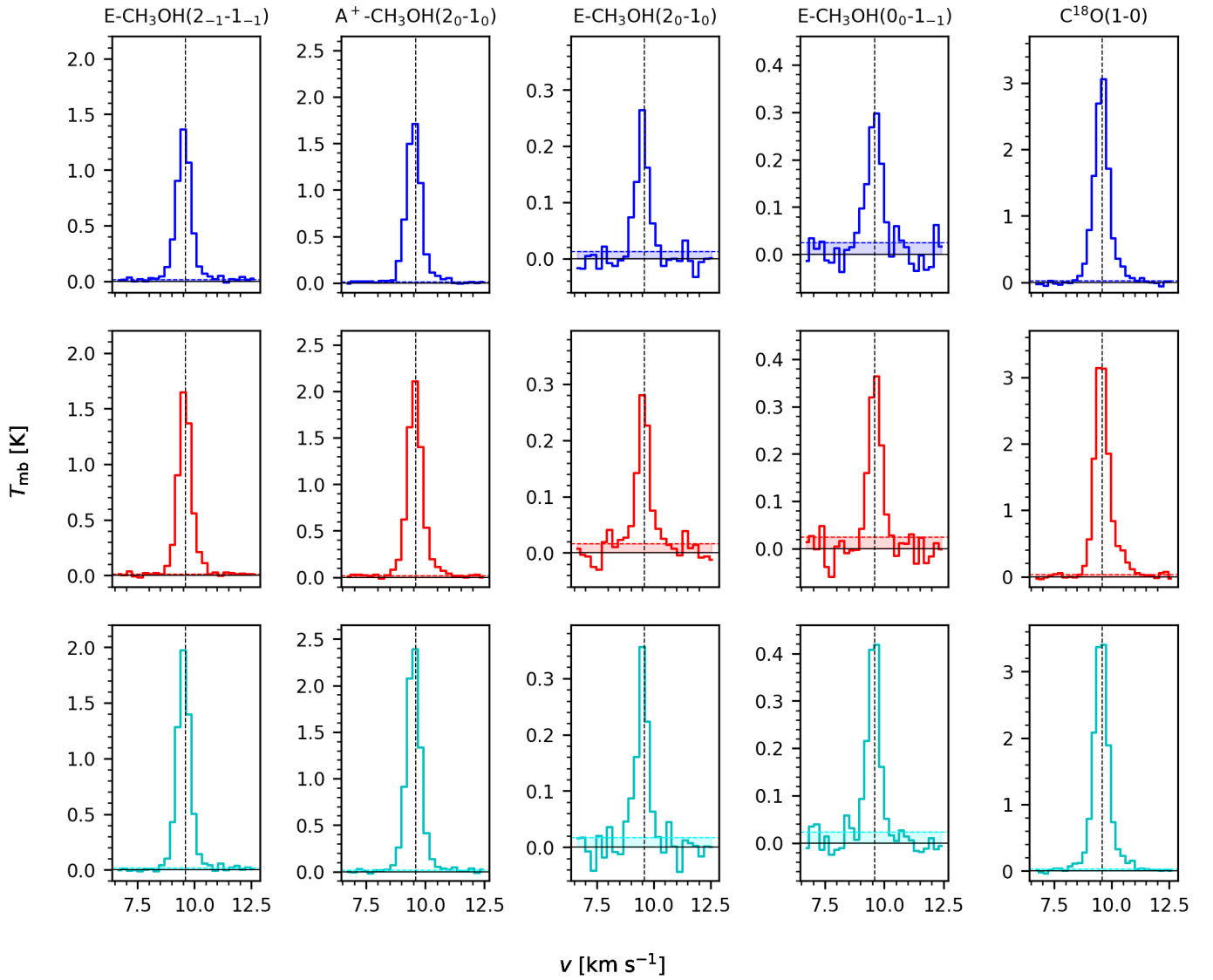


Fig. D.2: Spectral lines of CH<sub>3</sub>OH and C<sup>18</sup>O detected in the OSO 20 m data toward B5-Edge (top row), B5-East 189 (middle row), and B5-Hotspot (bottom row). The dashed vertical black line marks the assumed source LSR velocity (9.6 km s<sup>-1</sup>), and the shaded areas mark the calculated RMS noise levels as reported in Table D.2.

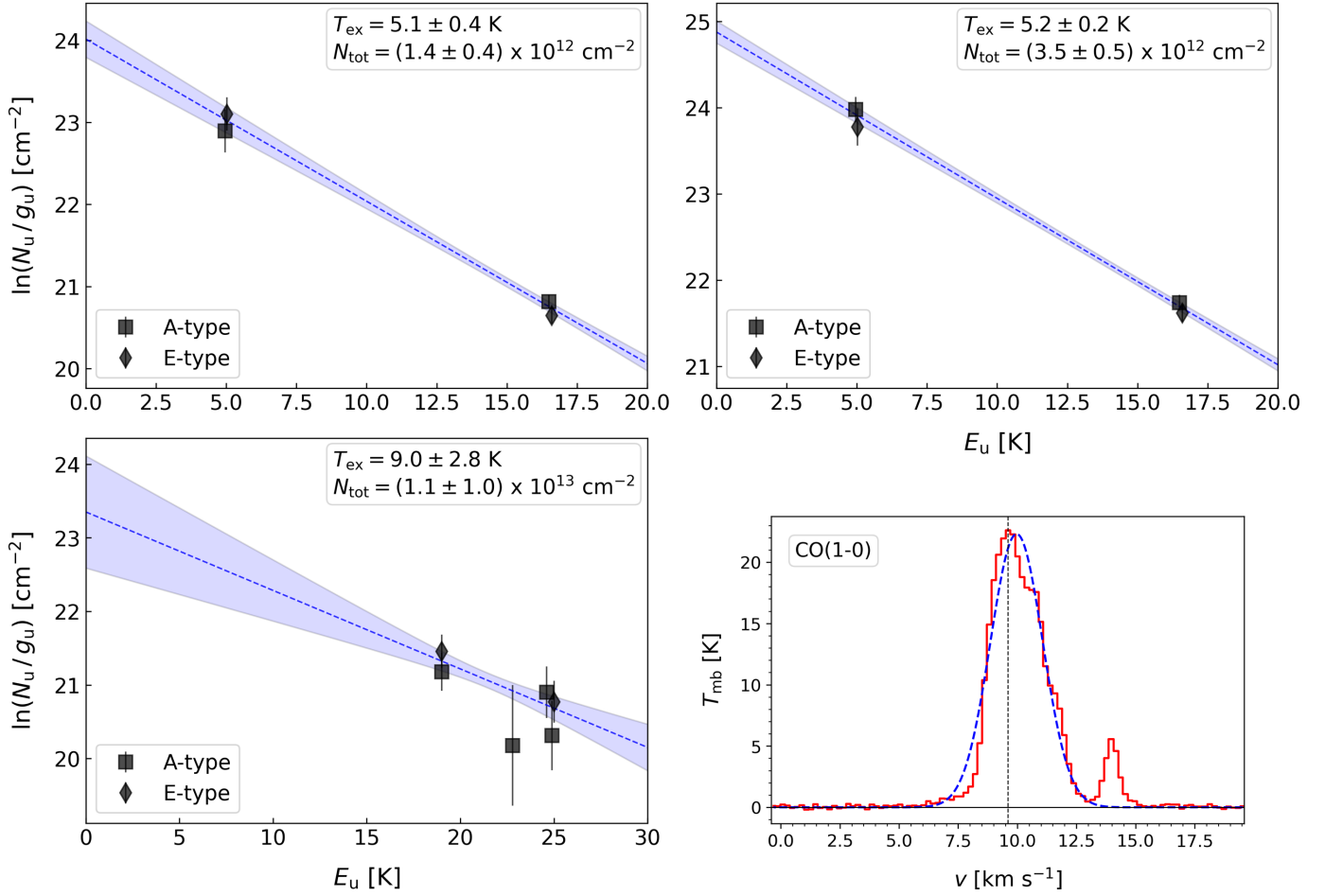


Fig. D.3: Rotation diagrams for acetaldehyde (CH<sub>3</sub>CHO) for B5-Edge (top left panel) and B5-East 189 (top right panel), and for methyl formate (CH<sub>3</sub>OCHO) for B5-East 189 (bottom left panel). In each of these panels, the dashed blue line marks the best linear fit to the data points, while the shaded blue area marks the 1 $\sigma$  confidence interval. Bottom right panel: CO(1-0) line measured toward B5-Hotspot with the OSO 20 m telescope on 09 October 2025 using frequency switching. The on-source integration time was  $\sim 1.9$  h. The dashed vertical black line marks the assumed source LSR velocity (9.6 km s<sup>-1</sup>), and the dashed blue line marks the best fit Gaussian. The emission feature next to the target line is the mesospheric CO(1-0) line.

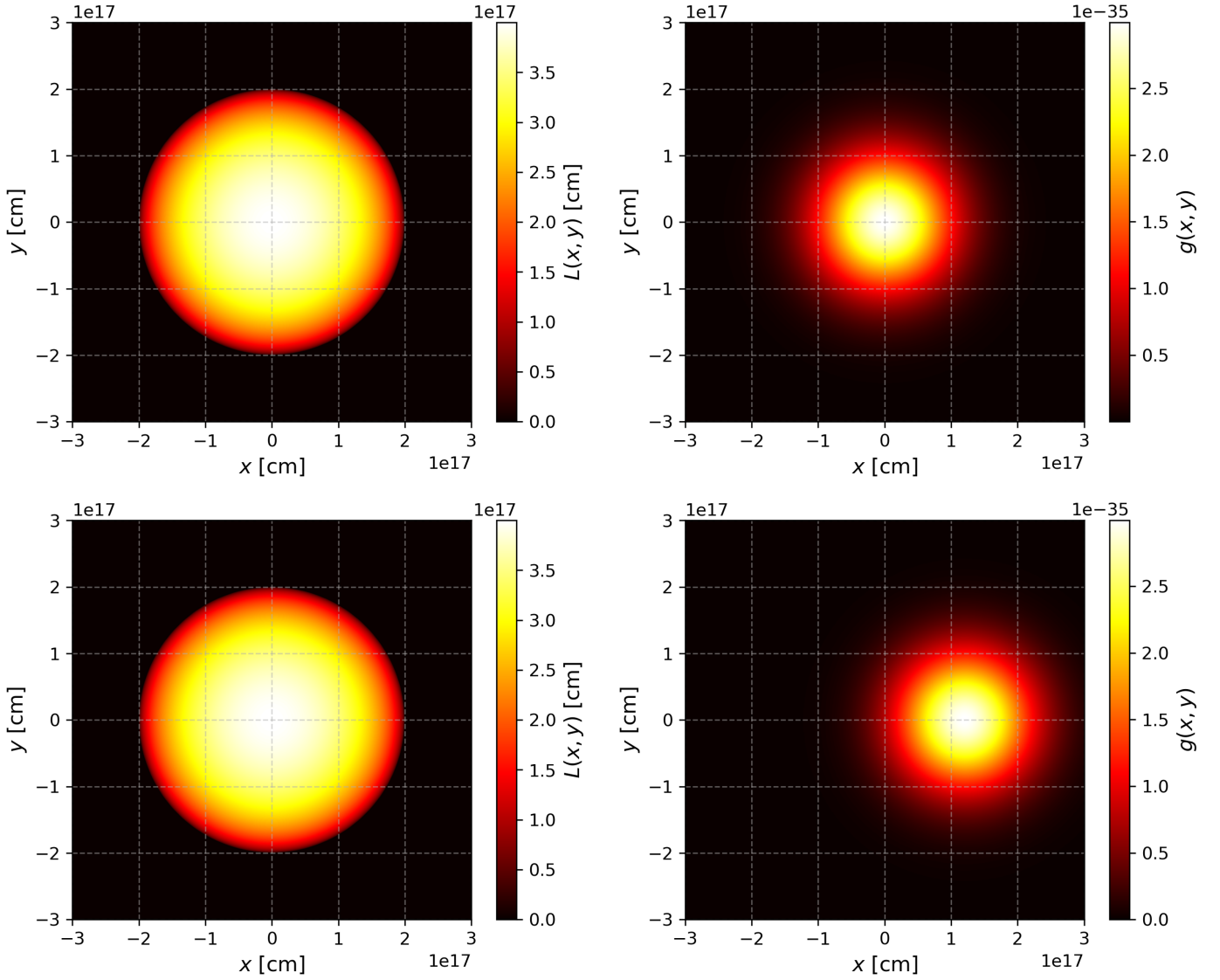


Fig. D.4: Chord length  $L(x, y)$  and beam shape function  $g(x, y)$  calculated from Eqs. (B.3) and (B.4), respectively, for a grid of  $(x, y)$  values (in cm). We assume  $R = 2 \times 10^{17}$  cm,  $D = 302$  pc, and  $\theta_{\text{arcsec}} = 38''$ . The panels in the top row show the beam convolution for B5-Hotspot and B5-East 189 in which the beam is centered at  $\mathbf{r} = (0, 0)$ , while the panels in the bottom row show the beam convolution for B5-Edge in which the beam is centered at  $\mathbf{r} = (0.6R, 0)$ .